

1     **Occurrence frequency of subcritical Richardson number**  
2     **assessed by global high-resolution radiosonde and ERA5**  
3             **reanalysis**

4  
5     Jia Shao<sup>1</sup>; Jian Zhang<sup>2\*</sup>; Wuke Wang<sup>3</sup>; Shaodong Zhang<sup>4</sup>; Tao Yu<sup>2</sup>; Wenjun Dong<sup>5,6</sup>

6  
7  
8     <sup>1</sup> College of Informatics, Huazhong Agricultural University, Wuhan 430070, China

9     <sup>2</sup> Hubei Subsurface Multi-scale Imaging Key Laboratory, School of Geophysics and  
10         Geomatics, China University of Geosciences, Wuhan 430074, China

11    <sup>3</sup> School of environmental studies, China University of Geosciences, Wuhan 430074,  
12         China

13    <sup>4</sup> School of Electronic Information, Wuhan University, Wuhan 430072, China

14    <sup>5</sup> Center for Space and Atmospheric Research (CSAR), Embry-Riddle Aeronautical  
15         University, Daytona Beach, FL, USA

16    <sup>6</sup> Global Atmospheric Technologies and Sciences (GATS), Boulder, CO, USA

17  
18  
19  
20    Correspondence to:

21    Dr. Jian Zhang (Email: [zhangjian@cug.edu.cn](mailto:zhangjian@cug.edu.cn))

29 **Abstract.** Kelvin Helmholtz instability (KHI) is most likely to be the primary source  
30 for clear-air turbulence that is of importance in pollution transfer and diffusion and  
31 aircraft safety. It is indicated by the critical value of the dimensionless Richardson ( $Ri$ )  
32 number, which is predicted to be  $1/4$  from linear stability analysis. However,  $Ri$  is fairly  
33 sensitive to the vertical resolution of the dataset; a higher resolution systematically  
34 leads to a finer structure. The study aims to evaluate the performance of ERA5  
35 reanalysis in determining the spatial-temporal variabilities of subcritical  $Ri$  by  
36 comparing it against a near-global high-resolution radiosonde dataset during years 2017  
37 to 2022 and further highlight global climatology and dynamical environment of  
38 subcritical  $Ri$ . Overall, the occurrence frequency of  $Ri < 1/4$  is inevitably underestimated  
39 by the ERA5 reanalysis over all climate zones at all heights from near-ground up to 30  
40 km, compared to radiosonde, due largely to the severe underestimation in wind shears.  
41 Otherwise, the occurrence frequency of  $Ri < 1$  in ERA5 is climatologically consistent  
42 with that from  $Ri < 1/4$  in radiosondes in the free troposphere, especially over the  
43 midlatitude and subtropics in the Northern/Southern Hemisphere. Therefore, we argue  
44 that threshold value of  $Ri$  could be approximated as 1 rather than  $1/4$  when using ERA5-  
45 based  $Ri$  as proxy for KHI. The occurrence frequency of subcritical  $Ri$  revealed by both  
46 datasets exhibits significant seasonal cycles over all climate zones. In addition, it is  
47 positively correlated with the standard derivation of orography at low-levels and is  
48 exceptionally strong over the Niño 3 region at heights of 6–13 km. Furthermore, high  
49 occurrence of subcritical  $Ri$  would likely be accompanied by strong wind speeds and  
50 intensive orographic or non-orographic gravity waves.

51

52 **Key words:** High-resolution radiosonde; ERA5 reanalysis; Wind shears; Richardson  
53 number; Gravity waves

54

55

56

## 57 **Introduction**

58 Kelvin Helmholtz instability (KHI) is a common phenomenon in the atmospheric  
59 boundary layer and the free atmosphere (Muschinski and Wode, 1998), and its  
60 wavelengths and depths span a wide range of scales throughout the atmosphere, varying  
61 from few meters or less to 10s of km (Fritts et al., 2011). It contributes to vertical mixing  
62 of heat, momentum, and constituents, and it acts to limit the maximum shears, just to  
63 name a few (Fritts et al., 2011). KHI along with gravity wave (GW) breaking are the  
64 most recognized instabilities in stably stratified flows (Fritts and Rastogi, 1985). KHI  
65 arises preferentially from micro- and mesoscale wind shear intensification, with  
66 maximal occurrence frequency near synoptic scale upper-level frontal zones near jet  
67 streams, with mountain waves, and above the tops of severe thunderstorms (North et  
68 al., 2014). Large wind shear is commonly associated with regions where stability  
69 changes rapidly (e.g., near the top of the boundary layer) and the large wind gradient in  
70 jet stream (Grasmick and Geerts, 2020). In a changing climate, wind shear in the North  
71 Atlantic upper-level jet stream could be increased (Lee et al., 2019), which may  
72 increase clear-air turbulence at cruise altitudes. In turn, KHI can reduce wind shears  
73 and alter tracer gradients where turbulence and mixing are most intense (Fritts et al.,  
74 2022).

75 KHI influences depend on the spatial scales at which they lead to turbulence (Fritts  
76 et al., 2022). Turbulence is by far the most common cause of serious injuries to aircraft  
77 (Williams and Joshi, 2013). Convective instability, shear instability, KHI, and GW  
78 breaking are known to be the major sources for turbulence (Sharman et al., 2012; Ko et  
79 al., 2019; 2022; [Lazarus et al., 2021](#)). KHI requires a sufficiently large Reynolds  
80 number and a Richardson ( $Ri$ ) number sufficiently below  $1/4$  to enable KHI formation  
81 and subsequent secondary instability leading to turbulence (Fritts et al., 2022).  $Ri$  is not  
82 a good guide to instability character in general, and  $Ri > 1/4$  does not assure flow stability  
83 for superpositions of mean and GW motions. Despite these caveats,  $Ri < 1/4$  does  
84 provide a reasonable guide to expected local KHI structure in cases where clear KH

85 billows arise, according to the simulation in the mesosphere and lower thermosphere  
86 region (Fritts et al., 2014). Values of  $Ri$  close to zero favor strong instability, deep  
87 billows, and relatively intense turbulence, whereas values of  $Ri$  closer to 1/4 favor weak  
88 instability, shallow billows (Fritts et al., 2011). The Richardson number criterion can  
89 be applied as a turbulence diagnostic in numerical model output (e.g. Sharman and  
90 Pearson, 2017), and it has been used as such in climatological studies on the occurrence  
91 of clear air turbulence (Jaeger and Sprenger, 2007). Kunkel et al. (2019) includes a brief  
92 discussion on the capability of ECMWF models based on case studies to resolve  
93 subcritical Richardson numbers, and argues that the threshold value of  $Ri$  ( $Rit$ ) taken as  
94 1 might be a good proxy for observed KHI. A very recent study by Lee et al. (2023)  
95 also sets  $Rit$  from 0–1 in their climatology on the upper troposphere and lower  
96 stratosphere turbulence diagnostics. Moreover, Zhang et al. (2022) shows that over half  
97 of turbulence exists below  $Ri < 1$  when the environment is beneficial for the development  
98 of turbulence.

99 Turbulent mixing is of crucial importance to mass, energy, momentum transfer, the  
100 dispersion of pollutants, and stratosphere-troposphere exchange. In numerical models,  
101 turbulent dissipation rate, turbulent diffusivity and other parameters representing  
102 turbulent mixing efficiency are the most basic parameters, which need to be accurately  
103 parameterized to evaluate the impact of turbulence effect on matter and energy  
104 distribution (Gavrilov et al., 2005). However, due to the intermittent nature of  
105 turbulence it is generally not resolved in (global) numerical weather prediction models,  
106 even at nowadays common/states of the art horizontal resolutions of the order of tens  
107 of kilometers (Sandu et al., 2019), and it presents a challenge both in observation and  
108 numerical modeling (Sharman et al., 2012; Homeyer et al., 2014; Plougonven and  
109 Zhang, 2014). For this reason, the indices of turbulence, such as large wind shear, small  
110  $Ri$  and the negative squared Brunt-väisälä frequency, could be a great tool to  
111 characterize turbulence (Jaeger et al., 2007).

112 The Richardson number is estimated by the finite differences across thin layers and  
113 is quite sensitive to the vertical resolution of measurements (Haack et al., 2014). Thus,  
114 a proper estimation of  $Ri$  requires a high-resolution measurement of temperature and

115 wind speed. The near-global distributed radiosonde site offers a unique opportunity to  
116 investigate the climatology of subcritical  $Ri$  occurrence frequency. The overview of  
117 subcritical  $Ri$  occurrence by using a near-global high-resolution (10-m) radiosonde data  
118 was presented in Zhang et al. (2022), and a close association between subcritical  $Ri$   
119 occurrence frequency and turbulence fraction has been found. However, the global  
120 climatology characteristic of subcritical  $Ri$  remains most unclear, especially over  
121 oceans where the radiosonde network has a poor coverage.

122 By comparison, ERA5 global reanalysis can provide a seamless coverage of  
123 temperature and wind, and it is the ~~latest generation~~ [latest version](#) of the European  
124 Centre for Medium-Range Weather Forecasts (ECMWF) [atmospheric reanalysis and is](#)  
125 [based on the state-of-the-art Integrated Forecasting System \(IFS\) Cy41r2 \(Hersbach et](#)  
126 [al., 2020; Gu et al., 2023\)](#) ~~has 137 model levels (Hersbach et al., 2020)~~. Its predecessor,  
127 ERA-Interim, was found in particular wind shear a factor of 2–3 lower simulated based  
128 on high-resolution radiosondes (Houchi et al., 2010). Moreover, results show that  
129 whatever the location and the geophysical conditions considered, biases between ERA-  
130 Interim and balloon wind measurements increase as a function of altitude (Duruiseau  
131 et al., 2017). Recent studies have suggested that the structure and variability of the trade  
132 winds in the lower troposphere are reasonably reproduced in the ERA5 reanalysis based  
133 on the EUREC4A field campaign (Savazzi et al., 2022). However, the similar  
134 comparison between ERA5 and high-resolution radiosonde across a near-global area  
135 has largely been undetermined. The proper estimation of wind shear and Brunt-Väisälä  
136 frequency is essential for the determination of  $Ri$ .

137 Thus, our objectives are to: (1) Evaluate the performance of ERA5 at different  
138 heights and climate zones in estimating wind shear and small Richardson number  
139 occurrence frequencies, in comparison with a large high-resolution radiosonde dataset  
140 spanning the years from 2017 to 2022. (2) Based on the validation and comparison  
141 results, we pose a question: how to use ERA5 for subcritical  $Ri$  estimation? (3) The  
142 global climatology of subcritical  $Ri$  occurrence based on versatile measurements and  
143 model products. (4) The dynamic environment (GWs and mean flow) of subcritical  $Ri$ .  
144 These works would be valuable for the understanding of the global distribution of

145 subcritical  $Ri$ , and furthermore, turbulence fraction. To this end, this analysis is  
146 organized as follows. Section 2 shows the data and methods used. Section 3 represents  
147 the climatological variation of subcritical  $Ri$  and its comparison with radiosonde.  
148 Section 4 ends with a summary.

149

## 150 **2 Data and methods**

### 151 **2.1 High-resolution radiosonde dataset**

152 As described in Guo et al. (2021) and Zhang et al. (2022), a high vertical resolution  
153 radiosonde (HVRRS) dataset gained from several organizations was adopted, spanning  
154 January 2017 to October 2022, in a total of 5.8 years. The organizations include the  
155 China Meteorological Administration (CMA), the U.S National Oceanic and  
156 Atmospheric Administration (NOAA), the Global Climate Observing System (GCOS)  
157 Reference Upper-Air Network (GRUAN), the Centre for Environmental Data Analysis  
158 of the United Kingdom (CEDA), University of Wyoming, Deutscher Wetterdienst, and  
159 ECMWF. In total, around 0.95 million radiosonde profiles from 434 radiosonde stations  
160 released at regular synoptic times of 0000 UTC and 1200 UTC were collected to  
161 determine the value of  $Ri$ . These profiles were sampled at 0.5 Hz or 1 Hz, corresponding  
162 to a vertical resolution of approximately 10 m or 5 m. Thus, all the profiles were evenly  
163 interpreted to 10 m resolution in vertical by applying a cubic spline interpolation. In  
164 addition, the sounding with the burst height lower than 10 km above ground level (a.g.l.)  
165 was directly discarded for further study. Meteorological variables, including  
166 temperature and wind speed, were prepared for the  $Ri$  estimation.

167 One of the shortages of radiosonde measurements is its inadequate concentration  
168 over the polar and ocean regions (Xia et al., 2021). The geographical distribution of  
169 total profile number of each radiosonde station is demonstrated in Figure S1 in the  
170 supporting information. The released radiosoundings over Europe, the United States,  
171 and Australia have good geographical coverage and time duration. Over some islands

172 of oceans (e.g., the Pacific Ocean) there are dozens of stations that can provide high-  
173 resolution measurement. Over the polar regions, there are around thirty stations.

## 174 2.2 ERA5 reanalysis and the collocation procedure

175 ERA5 is the latest version of ECMWF meteorological reanalysis, benefiting from  
176 a decade of developments in model physics, core dynamics, and data assimilation  
177 (Hersbach et al., 2020). The wind and temperature fields are modelled by the ERA5  
178 reanalysis on a spatial resolution of 0.25° latitude/longitude and a temporal resolution  
179 of 1 hour. The reanalysis has 137 model levels, giving a vertical resolution of  
180 approximately 300 m in the middle and upper troposphere. The vertical resolution of  
181 ERA5 is illustrated in Figure S2. Compared to ERA5, the HVRRS does not provide  
182 global seamless observations. Thus, the collocation procedure between reanalysis and  
183 HVRRS goes as follows: (1) the matched grid of ERA5 reanalysis is the nearest  
184 neighbor of radiosonde station; (2) the regular synoptic start time of radiosonde and  
185 reanalysis needs to keep exact the same; (3) the ~~pressure coordinate of model level of~~  
186 reanalysis that follows a hybrid sigma-pressure coordinate, —is converted into  
187 geometric-geopotential heightaltitude to match with HVRRS.

188 In addition, the standard deviations of orography (SDOR) and the gravity wave  
189 dissipation due to the effects of stress associated with unresolved valleys, hills and  
190 mountains in ERA5 reanalysis are extracted.

191 The relative error between HVRRS-based and ERA5-based quantities is estimated  
192 by the ratio of deviations between HVRRS and ERA5 derived quantities to the HVRRS  
193 one.

## 194 2.3 The occurrence frequency of subcritical $Ri$ and its uncertainty

195 Based on a linear theory, the threshold  $Ri$  ( $Ri_t$ ) defines the threshold where the air  
196 flow changes from stability to turbulence, and it is usually suggested to be 1/4 (Haack  
197 et al., 2014).  $Ri$  is formulated as:

$$198 \quad Ri = \bar{N}^2 / \bar{S}^2 \quad (1)$$

199 where  $N$  is the Brunt-Väisälä frequency ( $\sqrt{\frac{g}{\theta} \frac{d\theta}{dz}}$ ),  $S$  is the vertical wind shear  
 200 ( $\sqrt{(\frac{dU}{dz})^2 + (\frac{dV}{dz})^2}$ ), and the overbar denotes a moving average in a 200-m binstep to  
 201 eliminate the influence of measurement noises and small-scale fluctuations, such as  
 202 turbulence and small-scale waves. For a vertical resolution of 10-m, the averaged  
 203 parameter at altitude  $i$  can be represented as  $\bar{A}(i) = \frac{1}{n} \sum_{j=i-10}^{i+10} A(j)$ , where  $A$  denotes  
 204 wind shear or Brunt-Väisälä frequency, and  $n$  is the number of vertical bin. In addition,  
 205 horizontal winds measured under radiosonde at the scale of a few tens of meters are  
 206 affected by the chaotic movements of the gondola due to the pendulum and to the  
 207 balloon's own movements (Ingleby et al., 2022). However, it is hard to quantify the  
 208 movement in present study. For 10-m radiosondes, the moving average in a step of 200-  
 209 m could offset the effect of chaotic movements, at least to some extent. In this case, the  
 210 matching quantities that include  $Ri$ , wind shear, and the Brunt-Väisälä frequency  
 211 between radiosonde and ERA5 profiles are actually handled in averaged 200 m  
 212 intervals.

213 The Richardson number calculated from Eq.(1) depends on the vertical resolution  
 214 of the underlying data, as well as on the averaging interval. Ultimately, this influences  
 215 the estimated occurrence frequency for subcritical Richardson numbers as a proxy for  
 216 KHI. We resample the HVRRS data to 50 m and 100 m, and range the length scale of  
 217 overbar from 100 m to 500 m, to diagnose the uncertainties raised by the length scale  
 218 of segments and the vertical resolution of dataset. As indicated in Figure 1, under the  
 219 same length scale of overbar, a sparser vertical grid inevitably leads to a lower  
 220 occurrence frequency of subcritical  $Ri$ . For instance, as the length scale set to 100 m,  
 221 the occurrence frequency of  $Ri < 1/4$  at 0–2 km above sea level (a.s.l.) decreases from  
 222 22% when vertical resolution is equal to 10 m to 16% for a vertical resolution of 50 m.  
 223 Moreover, a longer length-scale of segment generally yields a smaller occurrence  
 224 frequency. For example, as the vertical resolution of radiosonde is equal to 10 m, the  
 225 occurrence frequency at 10–15 km decreases from 9% when the length scale of segment  
 226 equals 100 m to 1% when it equals 500 m. It is interesting to note that the occurrence  
 227 frequency under a vertical resolution of 50 m and a segment interval of 100 m is a bit

带格式的: 字体: (默认) Times New Roman, 小四

带格式的: 字体: 小四

带格式的: 字体: 小四

带格式的: 字体: 小四

带格式的: 字体: 小四

带格式的: 字体: 小四

带格式的: 字体: 小四

带格式的: 字体: 小四

带格式的: 字体: 小四

带格式的: 字体: 小四

带格式的: 字体: (默认) Times New Roman, 小四

带格式的: 字体: (默认) Times New Roman, 小四, 倾斜

带格式的: 字体: (默认) Times New Roman, 小四

带格式的: 字体: (默认) Times New Roman, 小四

带格式的: 字体: (默认) Times New Roman, 小四, 倾斜

带格式的: 字体: (默认) Times New Roman, 小四

带格式的: 字体: (默认) Times New Roman, 小四

带格式的



228 larger than that under a vertical resolution of 10 m and a segment of 200 m, possibly  
229 implying the fact that a shorter segment interval could be expected for a sparser vertical  
230 resolution.

## 231 2.4 Gravity wave energy

232 The GW energy is extracted based on the broad spectral method, according to Wang  
233 and Geller (2003). In this method, the magnitude of measured zonal wind ( $u$ ),  
234 meridional wind ( $v$ ), and temperature ( $T$ ) consisting of background states ( $u_0$ ,  $v_0$  and  
235  $T_0$ ) that are determined by applying a second-order polynomial fit (Chen et al., 2018;  
236 Zhang et al., 2022) and perturbations. Therefore, total perturbations are derived as:

$$237 \quad (u', v', T') = (u, v, T) - (u_0, v_0, T_0) \quad (2)$$

238 The perturbations could include measurement noises, KH waves, GWs, and  
239 planetary waves. Only the perturbations with vertical wavelengths of 0.3–6.9 km are  
240 considered as GWs (Wang and Geller, 2003). The mean vertical wavelength of GWs is  
241 about 2 km (Wang et al., 2005), and therefore, the lowermost threshold of 0.3 km could  
242 have little influence on the GW energy. However, the retrieval of the largest wavelength  
243 is not well determined, which is acknowledged as the radiosonde's "observational filter"  
244 (Alexander, 1998). By applying this band-pass filter, the average gravity-wave kinetic  
245 energy per unit mass (energy density) and the average potential energy density can be  
246 expressed as:

$$247 \quad E_k = \frac{1}{2} [\overline{u'^2} + \overline{v'^2}] \quad (3)$$

$$248 \quad E_p = \frac{1}{2} \frac{g^2 \overline{\hat{T}'^2}}{N^2} \quad (4)$$

249 where  $g$  is the gravitational constant,  $\hat{T}' = T'/\bar{T}$  the normalized perturbation  
250 temperature, and the overbar indicates an averaging over the tropospheric segment,  
251 which is chosen as 2–8.9 km for all regions, except the polar region, and it is selected  
252 as 2–7.4 km for the polar region (Wang and Geller, 2003). Eventually, the total GW  
253 energy  $E_t$  is the sum of  $E_k$  and  $E_p$ .

## 254 3 Results and Discussions

### 255 3.1 Comparisons of wind shear between HVRRS and ERA5 reanalysis

256 The variations in vertical shear of horizontal wind speed and the squared Brunt-  
257 väisälä frequency entirely determine the  $Ri$  magnitude. Figure 2 provides an overview  
258 of the spatial distribution of wind shear at heights of 0–2 km a.g.s.l. and 10–15 km a.g.s.l.  
259 obtained from the HVRRS and ERA5 reanalysis. HVRRS-based wind shear is taken  
260 from Eq.(1), with a vertical resolution of 10-m. The shear at heights of 0–2 km a.g.s.l.  
261 estimated by ERA5 reanalysis demonstrates a strong spatial variation, and it is largely  
262 dependent on underlying terrains and latitudes (Fig.2a). For example, large values can  
263 most likely be observed along the coastline, which could be attributed to the prevailing  
264 sea-breeze circulation. As compared to the HVRRS, these shears are slightly  
265 underestimated by ~~3.305-37~~ m/s/km, based on all sounding measurements (Fig.2b).  
266 Nevertheless, a close association between averaged ERA5-retrieved shears and  
267 HVRRS-determined shears can be noticed in terms of geospatial distribution, with a  
268 correlation coefficient of ~~0.4836~~ (Fig. 2b).

269 It is noteworthy that shear in the ERA5 reanalysis at heights of 10–15 km a.g.s.l. is  
270 significantly underestimated compared to the HVRRS, especially at middle latitudes,  
271 with a mean absolute error for all stations of about ~~87.408~~ m/s/km (Table 1). The  
272 underestimation could partly be due to the coarse vertical resolution (around 300-m) in  
273 the ERA5 reanalysis in this height interval. However, the spatial distribution of the  
274 ERA5 shear still exhibits a significant positive correlation with the HVRRS shear, with  
275 a correlation coefficient of ~~0.4435~~ (Fig.2d).

276 Following Houchi et al. (2010), the monthly shears over seven typical climate  
277 zones are separately investigated (Fig. 3), which are defined as follows: polar (70 °–  
278 90 °), mid latitudes (40 °–70 °), subtropics (20 °–40 °), and tropics (20 °S–20 °N). Over the  
279 polar region in the Northern/Southern Hemisphere, HVRRS-based shears are  
280 exceptionally strong in the lower stratosphere compared to those in the troposphere  
281 (Fig.3a, g), which could be attributed to the stratospheric polar jet. However, the similar

282 altitude variation can hardly be found in ERA5-based shears that are dramatically  
283 underestimated by around ~~12.44~~ m/s/km in the lower stratosphere (Fig.3h, n, also seen  
284 in Table 1). The results in midlatitudes reach a similar conclusion (Fig.3b, f, i, m). Over  
285 subtropical regions, HVRRS-based shears are consistent strong at heights of 16–21 km  
286 a.g.s.l., just above the subtropical jet stream (Fig.3c, e). However, in the ERA5  
287 reanalysis, the region with consistently strong shears can be noticed at approximately  
288 16 km a.g.s.l. (Fig.3j, l), which is about 3 km lower than that in the HVRRS. One  
289 possible reason might be that the model fails to resolve the further increasing shear in  
290 the lower stratosphere. In the tropics, the signature of quasi-biennial oscillation (QBO)  
291 can be identified in the lower stratosphere (Fig.3d, k).

292 The comparison between HVRRS-based and ERA5-based shears at three typical  
293 regimes is tabulated in Table 1. These metrics highlight that ERA5-based shears are  
294 underestimated by approximately ~~3.924.55~~ m/s/km, ~~7.658.47.5~~ m/s/km, ~~11.9912.410~~  
295 m/s/km at heights of 0–2 km, 10–15 km, and 20–25 km a.g.s.l., respectively, which are  
296 roughly consistent with Houchi et al. (2010).

297 By comparison, the ERA5-acquired  $N^2$  averaged [over four height intervals \(e.g.,](#)  
298 [0–5, 5–10, 10–15, 15–20 km a.g.s.l.\) from the surface to 30 km a.s.l.](#) is reliably estimated  
299 at all heights, with a relative error of around ~~11~~4%, as illustrated in Figure S3. This  
300 finding indicates that the ERA5 reanalysis can properly present the static stability of  
301 the background atmosphere, but it is not properly coincident with radiosonde in terms  
302 of the small-scale variability of dynamical structures. Due to a lack of global  
303 measurement of the fine-structure of the upper-air wind, however, the accuracy of  
304 ERA5-resolved shears is hard to be globally validated.

### 305 3.2 Occurrence frequency of $Ri < 1/4$ in HVRRS and ERA5 reanalysis

306 As a prominent example, the monthly occurrence frequency of  $Ri < 1/4$  over the  
307 Corpus Christi station (27.77° N, -97.5° W) during years from January 2017 to  
308 October 2022 is illustrated in Figure 4. As a result, the monthly occurrence rate of  
309  $Ri < 1/4$  in the ~~planetary boundary layer (PBL) regime~~ [low troposphere](#) determined from

带格式的: 非突出显示

带格式的: 非突出显示

带格式的: 非突出显示

带格式的: 非突出显示

310 HVRRS is lower than the ERA5-based one, with mean values of around 10.6% and  
311 16.9%, respectively. In the lowermost 2 km, the vertical resolution of ERA5 reanalysis  
312 is less than 200 m, and it is less than the moving segment interval in Eq.(1). The high  
313 occurrence frequency in the low troposphere ~~-PBL regime~~ could be likely related to  
314 the negative or small  $N^2$ . Especially during the daytime, the planetary boundary layer  
315 (PBL) is well mixed due to strong turbulence induced by uprising thermals (Song et al.,  
316 2018). In addition, an obvious seasonal cycle of occurrence frequencies is revealed by  
317 HVRRS in the middle and upper troposphere and has a maximum in winter (December–  
318 January–February) and spring (March–April–May) seasons, which is consistent with  
319 the finding in Zhang et al. (2019). In the vicinity of jet streams, the occurrence  
320 frequency of  $Ri < 1/4$  is generally enhanced by large wind shears. However, the ERA5  
321 reanalysis does not provide such a seasonal cycle pattern, and the occurrence frequency  
322 of  $Ri < 1/4$  is significantly underestimated by around 8% (Fig.4b), which could be  
323 attributed to the underestimation in wind shears. In the lower stratosphere, both the  
324 HVRRS and ERA5 reanalysis provide a low estimation of occurrence frequencies, with  
325 a value of around 1%.

326 Furthermore, on a large spatial scale the occurrence frequency of  $Ri < 1/4$  retrieved  
327 by ERA5 reanalysis is remarkably underestimated in the free atmosphere, as compared  
328 to the HVRRS. The annual variation of the occurrence frequency of  $Ri < 1/4$  over seven  
329 climate zones at 10–to 15 km a.g.l. ~~at 10 to 15 km a.s.l.~~ indicated by HVRRS and ERA5  
330 reanalysis is further demonstrated in Figure 5. It is clearly seen that the occurrence  
331 frequency of  $Ri < 1/4$  provided by ERA5 reanalysis is underestimated in all months, over  
332 all climate zones, possibly implying that, in the free atmosphere, the threshold value of  
333  $1/4$  in Eq.(1) is too small for the ERA5 reanalysis to capture the occurrence of KHI.

334 However, the ERA5 reanalysis data is non-uniformly sampled in altitude. Its  
335 vertical resolution drops from about 100-m in the boundary layer to about 500-m in the  
336 lower stratosphere. In contrast, radiosondes have a vertical resolution of 10-m at all  
337 heights. Therefore, we selected four typical heights and vertically interpolated the  
338 radiosonde to the same height resolution as ERA5 for comparison. The four height  
339 intervals are 0.8–1.3 km, 2.2–3.2 km, 6–15 km and 20–21 km a.g.s.l., as shown in Table

340 2. In these height intervals, the vertical resolution of ERA5 is about 100-m, 200-m, 300-  
341 m and 400-m respectively. Even at the same vertical resolution, ERA5 still seriously  
342 underestimates the value of  $OF(Ri < 1/4)$  at all heights and all climate zones. These  
343 results indicate that the greatest difficulty in evaluating subcritical  $Ri$  with ERA5 is that  
344 its simulation of wind shears might be seriously underestimated compared with  
345 radiosonde. As illustrated in Table 3, even accounting for the fact that ERA5 has a  
346 comparable vertical resolution of radiosonde, wind shears in ERA5 reanalysis are still  
347 underestimated by around 50.31.9%, 48.750.7%, 43.64.5%, and 62.25% at 0.8–1.3 km,  
348 2.2–3.2 km, 6–15 km and 20–21 km a.g.s.l., respectively. In order to obtain an  
349 occurrence frequency of subcritical  $Ri$  from ERA5 reanalysis that is comparable with  
350 radiosonde-based  $OF(Ri < 1/4)$ , the  $Rit$  for ERA5 should be set larger than 1/4. For  
351 instance, at 0.8–1.3 km and 2.2–3.2 km a.g.s.l., the  $Rit$  equals 1 could be a proper choice  
352 for ERA5 reanalysis, rather than 1/4 (Table 2). More generally,  $0.5 < Rit < 1.5$  could be  
353 more suitable for ERA5 reanalysis, compared to  $Rit = 1/4$ .

354 Due to the huge change in the vertical resolution of ERA5, it could be difficult to  
355 interpolate ERA5 into uniform data vertically with a relatively high resolution.  
356 Therefore, the question posed here is, what is the proper threshold value of  $Ri$  in  
357 predicting the occurrence of KHI when using the ERA5 reanalysis, compared to  
358 HVRRS? The occurrence frequency of  $Ri < 1/4$  indicated by the HVRRS, the ERA5-  
359 determined occurrence frequencies produced by  $Ri < 0.25$ ,  $Ri < 0.5$ ,  $Ri < 1$ ,  $Ri < 1.5$ , and  
360  $Ri < 2$  at all heights up to 30 km a.g.s.l. are demonstrated in Figure 6. It is notable that  
361 over all climate zones and in the free atmosphere, occurrence frequencies of  $Ri < 0.25$   
362 and  $Ri < 0.5$  obtained from the ERA5 reanalysis are underestimated, but the frequencies  
363 of  $Ri < 1.5$  and  $Ri < 2$  are generally overestimated. The occurrence frequency of  $Ri < 1$   
364 gives a close estimation both in magnitude and spatial variation compared to HVRRS  
365 over all climate zones.

366 Furthermore, the correlation coefficients between HVRRS-determined  
367 occurrence frequency and the ERA5-determined frequencies indicated by different  
368 threshold values of  $Ri$  at height levels of 0 to 30 km are illustrated in Figure 7. It is  
369 worth noting that, in the troposphere, the ERA5-based frequencies indicated by  $Ri < 1$ ,

带格式的: 非突出显示

带格式的: 非突出显示

带格式的: 非突出显示

带格式的: 非突出显示

带格式的: 非突出显示

370  $Ri < 1.5$ , and  $Ri < 2$  are highly positively correlated with those from the HVRRS, with a  
371 correlation coefficient of around 0.6 over all climate zones. In the lower stratosphere,  
372 however, these coefficients rapidly decline to 0.1, which can be explained by the low  
373 occurrence frequency in this height regime.

374 Combined the findings in Figures 6 and 7, in the free troposphere, we can conclude  
375 that the ERA5-determined occurrence frequency of  $Ri < 1$  is closest to the frequency of  
376  $Ri < 1/4$  based on the HVRRS. In the free atmosphere, KHI is the dominant source for  
377 clear-air turbulence (CAT) that is a well-known hazard to aviation. Therefore, the global  
378 characterization of KHI occurrence frequency in the free atmosphere obtained from  
379 ERA5 reanalysis could be of importance for understanding the spatial-temporal  
380 variation of CAT. In the following sections, the occurrence frequency of subcritical  $Ri$   
381 (hereinafter  $OF(Ri < Rit)$ ) is based on  $Ri < 1$  in ERA5 reanalysis and  $Ri < 1/4$  in HVRRS,  
382 unless otherwise noted.

383 Finally, it is noteworthy that  $OF(Ri < Rit)$  includes the component of  $Ri < 0$  that  
384 indicates potential for convective instability. However, both ERA5 and HVRRS are  
385 difficult to totally avoid  $Ri < 0$  when calculating  $Ri$ . Therefore, we evaluated the  
386 proportion of  $Ri < 0$  in all  $Ri < Rit$  in the two datasets to evaluate the possible contribution  
387 from convection, as shown in Figure 8. For HVRRS, the proportion of  $OF(Ri < 0)$  drops  
388 sharply from about 40% in the [PBL region low troposphere](#) to about 18% at 5–15  
389 a.g.s.l.. Similarly, for ERA5 its proportion drops from about 40% in the lowermost part  
390 of the atmosphere to about 2% at 5–16 km a.g.s.l.. These findings indicate that, in the  
391 free atmosphere,  $OF(Ri < Rit)$  is mainly composed of  $OF(0 < Ri < Rit)$ , which implies that  
392 local instabilities constitute most of the dynamic instability.

### 393 **3.3 The $OF(Ri < Rit)$ climatology**

394 For a first hint the global distributions of  $OF(Ri < Rit)$  provided by the ERA5  
395 reanalysis at 0–2 km, [5–10 km](#), [10–15 km](#), and [15–20 km](#) a.g.s.l. and [10–15 km a.s.l.](#)  
396 are displayed in Figure 9.  $OF(Ri < Rit)$  in the [PBL region low troposphere](#) is considerably  
397 spatially heterogeneous. Over subtropical oceans in the Northern/Southern Hemisphere,

398 the intense  $OF(Ri < Rit)$  can be noticed and has a magnitude of around 50% (Fig.9a). In  
399 addition, over the Sahara Desert the  $OF(Ri < Rit)$  reaches as high as 65%. Interestingly,  
400 the spatial variation in  $OF(Ri < Rit)$  ensembled by years 2017 to 2022 keeps high  
401 consistency with that of planetary boundary layer height (PBLH) over oceans, such as  
402 the Pacific Ocean near Japan and the Atlantic Ocean near U.S., as shown in Figure S4.  
403 However, at 0–2 km a.g.s.l., the spatial variation of  $OF(0 < Ri < Rit)$  exhibits a large  
404 difference with that of  $OF(Ri < Rit)$  in terms of magnitude, as shown in Figure S5. It is  
405 around 40% (20%) lower than that of  $OF(Ri < Rit)$  over subtropical oceans (Australia  
406 and North Africa). At heights of 5–10 km a.g.s.l., intensive  $OF(0 < Ri < Rit)$  can be  
407 viewed over the subtropic regions and has a value of around 10% (Fig.9b), which is  
408 likely attributed to upper tropospheric jets. In the upper troposphere over the  
409 tropical oceans,  $OF(Ri < Rit)$  is as high as 30% (Fig.9c), possibly as a result of the  
410 maximal heating effect by mesoscale convective systems (e.g., Houze 1982). In the  
411 lower stratosphere,  $OF(Ri < Rit)$  sharply decreases to around 0.1% (Fig.9d).–

412 In comparison, the spatial-temporal variability of  $OF(Ri < Rit)$  indicated by HVRRS  
413 keeps highly consistency with that of ERA5 reanalysis over all climate zones and in the  
414 free troposphere, except in the stratosphere of polar region (Figure 10). Seasonal cycles  
415 can be detected by both the HVRRS and ERA5 reanalysis over all climate zones,  
416 especially over subtropics and midlatitude regions. However, the ERA5-based  
417  $OF(Ri < Rit)$  can only reflect the large scale structure of the cycles, and it is hard to  
418 quantify the detailed variation like the HVRRS does.

419 Furthermore, the seasonal variation of  $OF(Ri < Rit)$  with  $Rit=1/4$  for HVRRS and  
420  $Rit=1$  for ERA5 for all climate zones is further analyzed in Figure 11. In the  
421 midlatitudes and subtropics, the  $OF(Ri < Rit)$  exhibits maximum values in the low  
422 tropospherePBL, as well as a local minimum in the middle troposphere and a local  
423 maximum at altitudes around 9 km. In the stratosphere the occurrence frequencies  
424 decrease to values of the order of 1% (Fig.11b,c,e,f). Over tropic regions, a primary  
425 peak can be clearly noticed at around 13 km, with a maximum of 12% for the HVRRS  
426 and 20% for the ERA5 reanalysis (Fig.11d, k). The seasonality over the tropical region  
427 could be related to some large scale flow features like the Summer Asian Monsoon and

428 the tropical easterly jet (Roja Raman et al., 2009; Sunilkumar et al., 2015; Kaluza et al.,  
429 2021). Over polar regions, the tropospheric  $OF(Ri < Rit)$  is significantly lower than that  
430 over other climate zones, with values ranging from around 4% at heights of 2–8 km to  
431 1% in the lower stratosphere (Fig. 11a,g).

432 In Table 4, the mean  $OF(Ri < Rit)$  magnitudes over seven climate zones and at three  
433 typical altitude regimes are listed. At 0–2 km a.g.s.l., the ERA5-based  $OF(Ri < Rit)$  is  
434 about 240% larger than that of the HVRRS-based one. At 10–15 km a.g.s.l., the ERA5-  
435 based  $OF(Ri < Rit)$  is reasonably well estimated, except that it is overestimated by  
436 around 5.928% over the tropics region. In addition, ERA5 underestimates  $OF(Ri < Rit)$   
437 by around 0.5% in the lower stratosphere.

438 According to Fig. 9a, it seems that low-level continental  $OF(Ri < Rit)$  is dependent  
439 on underlying terrains. ~~W. However, the vertical resolution of ERA5 in the PBL  
440 decreases sharply, leading to the fact that the resolution of the PBL data over the region  
441 with high elevations can be significantly lower than that of regions with low elevations,  
442 which could bring great challenges to the analysis of the impact of topography on low-  
443 level  $OF(Ri < Rit)$ . Therefore, we~~ investigate the association of low-level HVRRS-  
444 determined  $OF(Ri < Rit)$  with the standard deviation of orography (SDOR). At heights  
445 of 1–2 km a.g.l., the underlying terrain with a large SDOR generally corresponds to a  
446 high  $OF(Ri < Rit)$ , with a correlation coefficient between  $OF(Ri < Rit)$  and SDOR of 0.24.  
447 Then, the coefficient decreases to 0.15 at 3–4 km a.g.l. (Fig. 12b), and eventually, it  
448 equals 0.14 at 5–6 km a.g.l. (Fig. 12c). These findings indicate that, complex terrain  
449 may locally enhance  $OF(Ri < Rit)$ .

450 Moreover, it is quite evident from Fig. 9b and Fig. S5 that both  $OF(Ri < Rit)$  and  
451  $OF(0 < Ri < Rit)$  are largely enhanced over the tropical ocean associated with the El Niño  
452 Southern Oscillation (ENSO). The most of the enhanced  $OF(Ri < Rit)$  can be identified  
453 over the Niño 3 region (5°N–5°S, 150°W–90°W), and the time-height cross section  
454 of  $OF(Ri < Rit)$  during years of 2000 to 2022 is illustrated in Figure 13. The  $OF(Ri < Rit)$   
455 at height region of 6–13 km are evidently large, with values of around 3540%, which  
456 is about 1520% larger than the climatological mean value (Fig. 10k). More specifically,  
457  $OF(Ri < Rit)$  during time periods of La Niña events is obviously stronger than that during

带格式的: 非突出显示

带格式的: 字体颜色: 自动设置

带格式的: 字体颜色: 自动设置



458 the El Niño periods. The identification of ENSO events is based on Ren et al. (2018),  
459 Li et al. (2022), and Lv et al. (2022). It is also worth recalling here that the wind shear  
460 does not exhibit such an anomaly over the Niño 3 region (Fig.2c), implying that the  
461  $OF(Ri < Rit)$  anomaly could likely be attributed to the ENSO-related tropical convective  
462 heating in the upper troposphere, leading to a low Brunt-Väisälä frequency.

### 463 3.4 The dynamical environment of $OF(Ri < Rit)$ in the free troposphere

464 In the free troposphere the percentage of  $OF(Ri < 0)$  relative to  $OF(Ri < Rit)$  is  
465 generally less than 20% (Fig. 8) where the convection activity is generally weak, KHI  
466 is preferentially generated from strong wind shear, which may be closely associated  
467 with mean flows and wave activities.

468 The propagation of GW could raise strong wind shear, and therefore generate KHI.  
469 Thereby, we investigate the joint distribution of  $OF(Ri < Rit)$  with tropospheric GW total  
470 energy and wind shear (Figure 14). The latitudinal variation of GW total energy exhibits  
471 a double-peak structure, with two peaks at around  $30^\circ$  in the Northern/Southern  
472 Hemisphere (Fig.14a). The joint distribution of  $OF(Ri < Rit)$  with GW energy and wind  
473 shear indicates that large  $OF(Ri < Rit)$  (for instance, larger than 10%) generally  
474 corresponds to GW energy larger than 10 J/kg or wind shear exceeds 14 m/s/km (Fig.  
475 14b). Also,  $OF(0 < Ri < Rit)$  exhibits a similar distribution (Figure S6). Overall,  
476  $OF(Ri < Rit)$  obviously increases with GW total energy (Figure S9a), possibly implying  
477 that the propagation of GWs could enhance wind shear and therefore, the burst of KHI.

478 In addition, the interaction between low-level wind and mountain barrier could be  
479 a source of orographic GWs (Zhang et al., 2022). We take orographic GW dissipation  
480 in ERA5 reanalysis, which is the accumulated conversion of kinetic energy in the mean  
481 flow into heat over the whole atmospheric column, as an indicator of the strength of  
482 orographic GWs. It is interesting to note that monthly averaged orographic GW  
483 dissipation and monthly ERA5-determined  $OF(Ri < Rit)$  at heights from ground up to 30  
484 km demonstrates a close association (Figure S7). For instance, in the middle  
485 troposphere, they are positively associated over mountainous areas such as the Rocky

带格式的: 字体: 倾斜

486 Mountains and the Alps Mountain, with correlation coefficients of around 0.5. These  
487 findings also suggest that during months with strong unresolved orographic gravity  
488 wave activity, which then modify the flow and stability parameters of the resolved flow,  
489 leading to a low Richardson number and result in an enhanced  $OF(Ri < Rit)$ . Nevertheless,  
490 it is hard to quantify the effect of resolved orographic GWs on  $Ri$  here.

491 ———  
492 At jet heights (10–15 km a.g.l.), a large shear can be easily induced by strong wind  
493 speed. Figure 15 demonstrates the joint distribution of  $OF(Ri < Rit)$  with wind speed and  
494 wind shear. Generally Similarly, large  $OF(Ri < Rit)$  larger than 10% ( $\rightarrow 10\%$ ) can be easily  
495 found when the wind speed-shear exceeds 20 25 m/s/km. In addition,  $OF(0 < Ri < Rit)$   
496 can draw a similar conclusion (Figure S8). In the middle and upper troposphere,  
497  $OF(Ri < Rit)$  almost linearly increases with wind speed (Figure S9b).

498 In a short conclusion, in the free troposphere, the occurrence of KHI would favor  
499 the dynamical environment with strong-intensive orographic or non-orographic GW  
500 activities and relatively large large mean flows (around 25 m/s).

#### 501 4 Conclusion and remarks

502 The occurrence of KHI is potential crucial for many implications, such as aircraft  
503 safety and mass transfer, but it is very hard to be globally understood due to its fine  
504 structure. The subcritical Richardson number is commonly used as an indicator for KHI.  
505 This study uses the ERA5 as the latest reanalysis product from the ECMWF as well as  
506 a comprehensive data set of HVRRS radiosonde soundings to globally characterize the  
507 distribution of low Richardson numbers as a proxy for the occurrence of KHI, for the  
508 years 2017 to 2022.

509 Vertical wind shears are considerably underestimated at almost all heights and over  
510 all climate zones by the ERA5 reanalysis, compared to the HVRRS. It is noteworthy  
511 that vertical wind shear in the ERA5 reanalysis at heights of 10–15 km a.g.l. is  
512 dramatically underestimated by around 7.6548 m/s/km, especially at middle latitudes.  
513 However, the spatial distribution of the ERA5 shear exhibits a statistically significant

514 positive correlation with the HVRRS shear. As a result, the ERA5-determined  
515 occurrence frequency of  $Ri < 1/4$  is significantly underestimated. In addition, it is weak  
516 correlated with HVRRS-determined ones at most heights and over most climate zones.

517 However, the vertical resolution of ERA5 reanalysis sharply decreases with altitude,  
518 which is not comparable with HVRRS. Thus, to match with ERA5 reanalysis at  
519 specified height intervals, the HVRRS was vertically interpolated with resolutions  
520 spanning from 100-m to 400-m. Even at a comparable resolution, vertical wind shear  
521 is underestimated by around 50%, leading to a considerable underestimation in  
522  $OF(Ri < 1/4)$ , compared to radiosondes.

523 Interestingly, the ERA5-determined occurrence frequency of  $Ri < 1$  is generally  
524 consistent with the frequency of  $Ri < 1/4$  obtained from HVRRS, in terms of magnitude  
525 and temporal variation. Rather than  $Ri < 1/4$ , we argue that the threshold value of  $Ri < 1$   
526 could be more proper when using ERA5 reanalysis for KHI study, especially in the  
527 middle and upper troposphere over midlatitude and subtropic regions in the  
528 Northern/Southern Hemisphere, where a high consistency between HVRRS and ERA5  
529 has been found in terms of  $OF(Ri < Rit)$  magnitude. In other words, under a similar  
530 occurrence frequency, the identification of vertical segments with  $Ri < 1$  in ERA5 is  
531 equitable with identification of vertical segments with  $Ri < 1/4$  using HVRRS. It is worth  
532 highlighting that HVRRS experiences a 200-m vertical moving average procedure to  
533 inhibit measurement noises and turbulence fluctuations. Without this procedure, the  
534 threshold  $Ri$  for the ERA5 reanalysis would even higher than 1. –

带格式的: 字体: 倾斜

535 The climatology of  $OF(Ri < Rit)$  exhibits significant seasonal cycles over all  
536 latitudes. A poleward decrease can be clearly identified in the middle and upper  
537 troposphere. In addition, over mountainous area, complex terrain may locally enhance  
538 low-level  $OF(Ri < Rit)$ . Moreover, it is immediately obvious that the both  $OF(Ri < Rit)$   
539 and  $OF(0 < Ri < Rit)$  in the middle and upper troposphere of the Niño 3 region is largely  
540 enhanced probably by the tropical convective heating.

541 Moreover, both  $OF(Ri < Rit)$  and  $OF(0 < Ri < Rit)$  exhibit close relationship with GW  
542 activities and background mean flow. For instance, large  $OF(Ri < Rit)$  ( $\rightarrow 10\%$ ) favors  
543 intensive GW activities energy larger than 10 J/kg and strong or-mean flow stronger than

544 ~~25 m/s~~. Over complex terrains, the orographic GW breaking could locally enhance  
545  $OF(Ri < Rit)$ .

546 Those findings are valuable for pointing out the performance of the ERA5  
547 reanalysis in terms of resolving low Richardson numbers as a proxy for KHI, in  
548 comparison with a near-global high-resolution radiosonde measurement. In addition,  
549 the spatial-temporal variability of  $OF(Ri < Rit)$  over different climate zones from near-  
550 ground up to 30 km is quantitatively characterized by ERA5 and HVRRS, which could  
551 provide new insights that increase our understanding of the fine structure of upper air.  
552

### 553 **Acknowledgement**

554 The authors would like to acknowledge the National Meteorological Information  
555 Centre (NMIC) of CMA, NOAA, Deutscher Wetterdienst (Climate Data Center), U.K  
556 Centre for Environmental Data Analysis (CEDA), GRUAN, ECMWF, and the  
557 University of Wyoming for continuously collecting and generously providing high-  
558 resolution radiosonde data. Last but not least, we would like to thank two anonymous  
559 reviewers for their excellent comments that greatly helped to improve our work.  
560

### 561 **Financial support**

562 This study jointly supported by the National Natural Science Foundation of China under  
563 grants 42205074, ~~42127805, and 62101203~~ and ~~42127805~~, the Hubei Provincial  
564 Natural Science Foundation of China under Grant 2021CFB459, and the Research  
565 Grants of Huazhong Agricultural University under grants No. 2662021XXQD002 and  
566 2662021JC008.  
567

568 **Competing interests**

569 The contact author has declared that neither they nor their co-authors have any  
570 competing interests

571

572 **Data availability**

573 The dataset can be accessed at ECMWF (2022).

574

575 **Author contributions**

576 JZ conceptualized this study. JS carried out the analysis with comments from other co-  
577 authors. JZ wrote the original manuscript. WW, SZ, TY, WD provided useful  
578 suggestions for the study. All authors contributed to the improvement of paper.

579

580 **References**

581 Alexander, M. J.: Interpretations of observed climatological patterns in stratospheric  
582 gravity wave variance, *J. Geophys. Res. Atmos.*, 103(D8), 8627–8640,  
583 <https://doi.org/10.1029/97JD03325>, 1998.

584 Duruisseau, F., N., Huret, A., Andral, and Camy-Peyret, C.: Assessment of the ERA-  
585 Interim winds using high-altitude stratospheric balloons, *J. Atmos. Sci.*, 74(6),  
586 2065–2080, <https://doi.org/10.1175/JAS-D-16-0137.1>, 2017.

587 ECMWF: ECMWF Reanalysis v5 (ERA5), European Centre for Medium-Range  
588 Weather Forecasts [data set],  
589 <https://www.ecmwf.int/en/forecasts/dataset/ecmwf-reanalysis-v5>, last access:  
590 07 December 2022.

591 Fritts, D. C., K. Wan, J. Werne, T. Lund, and Hecht, J. H.: Modeling the implications of  
592 Kelvin-Helmholtz instability dynamics for airglow observations, *J. Geophys.*  
593 *Res. Atmos.*, 119, 8858–8871, <https://doi.org/10.1002/2014JD021737>, 2014.

594 Fritts, D. C., P. M. Franke, K. Wan, T. Lund, and Werne, J.: Computation of clear-air  
595 radar backscatter from numerical simulations of turbulence: 2. Backscatter  
596 moments throughout the lifecycle of a Kelvin Helmholtz instability, *J. Geophys.*  
597 *Res.*, 116, D11105, <https://doi.org/10.1029/2010JD014618>, 2011.

598 Fritts, D. C., and Rastogi, P. K.: Convective and dynamical instabilities due to gravity  
599 wave motions in the lower and middle atmosphere: Theory and observations.  
600 *Radio Sci.*, 20, 1247–1277, <https://doi.org/10.1029/RS020i006p01247>, 1985.

601 Fritts, D. C., L., Wang, T. S., Lund, S. A., Thorpe, C. B., Kjellstrand, B., Kaifler, and  
602 Kaifler, N.: Multi-Scale Kelvin-Helmholtz instability dynamics observed by  
603 PMC Turbo on 12 July 2018: 2. DNS modeling of KHI dynamics and PMC  
604 responses., *J. Geophys. Res. Atmos.*, 127, e2021JD035834.  
605 <https://doi.org/10.1029/2021JD035834>, 2022.

606 Grasmick, C., and Geerts, B.: Detailed dual-Doppler structure of Kelvin–Helmholtz  
607 waves from an airborne profiling radar over complex terrain. Part I: Dynamic  
608 structure, *J. Atmos. Sci.*, 77(5), 1761–1782., [https://doi.org/10.1175/JAS-D-19-](https://doi.org/10.1175/JAS-D-19-0108.1)  
609 [0108.1](https://doi.org/10.1175/JAS-D-19-0108.1), 2020.

610 Gavrilov, N. M., Luce, H., Crochet, M., Dalaudier, F., and Fukao, S.: Turbulence  
611 parameter estimations from high-resolution balloon temperature measurements  
612 of the MUTSI-2000 campaign, *Ann. Geophys.*, 23, 2401–2413,  
613 [doi:10.5194/angeo-23-2401-2005](https://doi.org/10.5194/angeo-23-2401-2005), 2005

614 [Gu, L., Yin, J., Gentine, P. et al.: Large anomalies in future extreme precipitation](#)  
615 [sensitivity driven by atmospheric dynamics,- \*Nat. Commun.\*, 14, 3197, \(2023\).](#)  
616 <https://doi.org/10.1038/s41467-023-39039-7>, 2023.

617 Guo, J., Zhang, J., Yang, K., Liao, H., Zhang, S., Huang, K., Lv, Y., Shao, J., Yu, T.,  
618 Tong, B., Li, J., Su, T., Yim, S. H. L., Stoffelen, A., Zhai, P., and Xu, X.:  
619 Investigation of near-global daytime boundary layer height using high-  
620 resolution radiosondes: first results and comparison with ERA5, MERRA-2,

带格式的: 字体: (默认) Times New Roman, 小四, 图案: 清除 (白色)

621 JRA-55, and NCEP-2 reanalyses, *Atmos. Chem. Phys.*, 21, 17079–17097,  
622 <https://doi.org/10.5194/acp-21-17079-2021>, 2021.

623 Haack, A., M. Gerding, and Lübken, F.-J.: Characteristics of stratospheric turbulent  
624 layers measured by LITOS and their relation to the Richardson number, *J.*  
625 *Geophys. Res. Atmos.*, 119, 10605–10618,  
626 <https://doi.org/10.1002/2013JD021008>, 2014.

627 Hersbach, H., Bell, B., Berrisford, P., Hirahara, S., Horányi, A., Muñoz-Sabater, J.,  
628 Nicolas, J., Peubey, C., Radu, R., Schepers, D., Simmons, A., Soci, C., Abdalla,  
629 S., Abellan, X., Balsamo, G., Bechtold, P., Biavati, G., Bidlot, J., Bonavita, M.,  
630 De Chiara, G., Dahlgren, P., Dee, D., Diamantakis, M., Dragani, R., Flemming,  
631 J., Forbes, R., Fuentes, M., Geer, A., Haimberger, L., Healy, S., Hogan, R. J.,  
632 Hólm, E., Janisková, M., Keeley, S., Laloyaux, P., Lopez, P., Lupu, C., Radnoti,  
633 G., de Rosnay, P., Rozum, I., Vamborg, F., Villaume, S., and Thépaut, J.-N.: The  
634 ERA5 global reanalysis, *Q. J. Roy. Meteorol. Soc.*, 146, 1999–2049,  
635 <https://doi.org/10.1002/qj.3803>, 2020.

636 Homeyer, C. R., L. L. Pan, and Barth, M. C.: Transport from convective overshooting  
637 of the extratropical tropopause and the role of large-scale lower stratospheric  
638 stability, *J. Geophys. Res. Atmos.*, 119(5), 2220–2240,  
639 <https://doi.org/10.1002/2013JD020931>, 2014.

640 Houchi, K., Stoffelen, A., Marseille, G. J., and De Kloe, J.: Comparison of wind and  
641 wind shear climatologies derived from high-resolution radiosondes and the  
642 ECMWF model, *J. Geophys. Res.-Atmos.*, 115, D22123,  
643 <https://doi.org/10.1029/2009JD013196>, 2010.

644 Houze, R. A., Jr.: Cloud clusters and large-scale vertical motions in the tropics. *J.*  
645 *Meteor. Soc. Japan*, 60, 396–410, <https://doi.org/10.2151/jmsj1965.60.1.396>,  
646 1982.

647 Ingleby, B., Motl, M., Marlton, G., Edwards, D., Sommer, M., von Rohden, C., Vömel,  
648 H., and Jauhiainen, H.: On the quality of RS41 radiosonde descent data, *Atmos.*  
649 *Meas. Tech.*, 15, 165–183, <https://doi.org/10.5194/amt-15-165-2022>, 2022.

650 Lazarus, S. M., Chiappa, J., Besing, H., Splitt, M. E., and Riousset, J. A.: (2021).

带格式的: 字体: (默认) Times New Roman, 小四

带格式的: 字体: (默认) Times New Roman, 小四

带格式的: 字体: (默认) Times New Roman, 小四

651 [Distinguishing characteristics of the tropical cyclone gigantic jet environment.](#)  
652 [J. Atmos. Sci. Journal of the Atmospheric Sciences, 78\(9\), 2741–2761,](#)  
653 <https://doi.org/10.1175/JAS-D-20-0265.1>, 2021.

654 Lee, S. H., Williams, P. D., and Frame, T. H.: Increased shear in the North Atlantic  
655 upper-level jet stream over the past four decades, *Nature*, 572, 639–642,  
656 <https://doi.org/10.1038/s41586-019-1465-z>, 2019.

657 Lee, J. H., Kim, J.-H., Sharman, R. D., Kim, J., and Son, S.-W. Climatology of Clear-  
658 Air Turbulence in upper troposphere and lower stratosphere in the Northern  
659 Hemisphere using ERA5 reanalysis data, *J. Geophys. Res.-Atmos.-Journal of*  
660 *Geophysical Research: Atmospheres*, 128, e2022JD037679,  
661 <https://doi.org/10.1029/2022JD037679>, 2023.

662 Li, X., Hu, Z. Z., Tseng, Y. H., Liu, Y., and Liang, P.: A historical perspective of the La  
663 Niña event in 2020/2021, *J. Geophys. Res.-Atmos.*, 127(7), e2021JD035546,  
664 <https://doi.org/10.1029/2021JD035546>, 2022.

665 Lv, A., Fan, L., and Zhang, W.: Impact of ENSO Events on Droughts in China,  
666 *Atmosphere*, 13(11), 1764, <https://doi.org/10.3390/atmos13111764>, 2022.

667 Jaeger, E. B., and Sprenger, M.: A Northern Hemispheric climatology of indices for  
668 clear air turbulence in the tropopause region derived from ERA40 reanalysis  
669 data, *J. Geophys. Res.*, 112, D20106, doi:10.1029/2006JD008189, 2007.

670 Kaluza, T., Kunkel, D., and Hoor, P.: On the occurrence of strong vertical wind shear  
671 in the tropopause region: a 10-year ERA5 northern hemispheric study, *Weather*  
672 *Clim. Dynam.*, 2, 631–651, <https://doi.org/10.5194/wcd-2-631-2021>, 2021.

673 Kunkel, D., Hoor, P., Kaluza, T., Ungermann, J., Kluschat, B., Giez, A., Lachnitt, H.-  
674 C., Kaufmann, M., and Riese, M.: Evidence of small-scale quasi-isentropic  
675 mixing in ridges of extratropical baroclinic waves, *Atmos. Chem. Phys.*, 19,  
676 12607–12630, <https://doi.org/10.5194/acp-19-12607-2019>, 2019.

677 Ko, H. C., H. Y., Chun, R., Wilson, and Geller, M. A.: Characteristics of  
678 atmospheric turbulence retrieved from high vertical-resolution radiosonde  
679 data in the United States, *J. Geophys. Res. Atmos.*,  
680 124, <https://doi.org/10.1029/2019JD030287>, 2019.



681 Ko, H. C. and Chun, H. Y.: Potential sources of atmospheric turbulence estimated using  
682 the Thorpe method and operational radiosonde data in the United States. *Atmos.*  
683 *Res.*, 265, 105891, <https://doi.org/10.1016/j.atmosres.2021.105891>, 2022.

684 Muschinski, A., and Wode, C.: First in situ evidence for coexisting submeter  
685 temperature and humidity sheets in the lower free troposphere, *J. Atmos. Sci.*,  
686 55(18), 2893–2906, [https://doi.org/10.1175/1520-0469\(1998\)055<2893:FISEFC>2.0.CO;2](https://doi.org/10.1175/1520-0469(1998)055<2893:FISEFC>2.0.CO;2), 1998.

688 North, G. R., Pyle, J. A., and Zhang, F.: *Encyclopedia of atmospheric sciences*,  
689 Academic Press, Cambridge, Massachusetts, United States, 224 pp., 2014

690 Plougonven, R., and Zhang, F.: Internal gravity waves from atmospheric jets and fronts,  
691 *Rev. Geophys.*, 52, 33–76, <https://doi.org/10.1002/2012RG000419>, 2014.

692 Ren, H. L., B., Lu, J., Wan, B., Tian, and Zhang, P.: Identification standard for ENSO  
693 events and its application to climate monitoring and prediction in China, *J.*  
694 *Meteorol. Res.*, 32, 923–936, <https://doi.org/10.1007/s13351-018-8078-6>, 2018.

695 Roja Raman, M., Jagannadha Rao, V. V., Venkat Ratnam, M., Rajeevan, M., Rao, S. V.,  
696 Narayana Rao, D., and Prabhakara Rao, N.: Characteristics of the Tropical  
697 Easterly Jet: Long-term trends and their features during active and break  
698 monsoon phases, *J. Geophys. Res.-Atmos.*, 114, 1–14,  
699 <https://doi.org/10.1029/2009JD012065>, 2009.

700 Sandu, I., A., A., van Niekerk, T. G., Shepherd, S. B., Vosper, A., Zadra, J., Bacmeister,  
701 et al: Impacts of orography on large-scale atmospheric circulation. *npj Clim*  
702 *Atmos Sci*, 2(1), 1–8, <https://doi.org/10.1038/s41612-019-0065-9>, 2019.

703 Savazzi, A. C. M., Nuijens, L., Sandu, I., George, G., and Bechtold, P.: The  
704 representation of the trade winds in ECMWF forecasts and reanalyses during  
705 EUREC<sup>4</sup>A, *Atmos. Chem. Phys.*, 22, 13049–13066,  
706 <https://doi.org/10.5194/acp-22-13049-2022>, 2022.

707 Sharman, R. D., S. B. Trier, T. P. Lane, and Doyle., J. D.: Sources and dynamics of  
708 turbulence in the upper troposphere and lower stratosphere: A review, *Geophys.*  
709 *Res. Lett.*, 39, L12803, <https://doi.org/10.1029/2012GL051996>, 2012.

710 Sharman, R. D., and Pearson, J. M: Prediction of energy dissipation rates for aviation

711 turbulence. Part I: Forecasting nonconvective turbulence. *J. Appl. Meteorol.*  
712 *Climatol*, 56(2), 317–337, <https://doi.org/10.1175/JAMC-D-16-0205.1>, 2017.

713 Song, J., Z.-H., Wang, and Wang, C.: The regional impact of urban heat mitigation  
714 strategies on planetary boundary layer dynamics over a semiarid city, *J.*  
715 *Geophys. Res. Atmos.*, 123(12), 6410–6422,  
716 <https://doi.org/10.1029/2018JD028302>, 2018.

717 Sunilkumar, S. V., Muhsin, M., Parameswaran, K., Venkat Ratnam, M., Ramkumar,  
718 G., Rajeev, K., Krishna Murthy, B. V., Sambhu Namboodiri, K. V.,  
719 Subrahmanyam, K. V., Kishore Kumar, K., and Shankar Das, S.: Characteristics  
720 of turbulence in the troposphere and lower stratosphere over the Indian  
721 Peninsula, *J. Atmos. Sol.-Terr. Phys.*, 133, 36–53,  
722 <https://doi.org/10.1016/j.jastp.2015.07.015>, 2015.

723 Wang, L., and Geller, M. A.: Morphology of gravity-wave energy as observed from 4  
724 years (1998–2001) of high vertical resolution U.S. radiosonde data, *J. Geophys.*  
725 *Res. Atmos.*, 108(D16), 4489, <https://doi.org/10.1029/2002JD002786>, 2003.

726 Wang, L., Geller, M. A., and Alexander, M. J.: Spatial and Temporal Variations of  
727 Gravity Wave Parameters, Part I: Intrinsic Frequency, Wavelength, and Vertical  
728 Propagation Direction, *J. Atmos. Sci.*, 62, 125–142,  
729 <https://doi.org/10.1175/JAS-3364.1>, 2005

730 Williams, P. D., and Joshi, M. M.: Intensification of winter transatlantic aviation  
731 turbulence in response to climate change. *Nat. Clim. Chang.*, 3(7), 644–648,  
732 <https://doi.org/10.1038/nclimate1866>, 2013.

733 Xia, P., Y., Shan, S., Ye, and Jiang, W.: Identification of Tropopause Height with  
734 Atmospheric Refractivity, *J. Atmos. Sci.*, 78(1), 3–16  
735 <https://doi.org/10.1175/JAS-D-20-0009.1>, 2021.

736 Zhang, J., S. D., Zhang, C. M., Huang, K. M., Huang, Y., Gong, Q., Gan, and Zhang,  
737 Y. H.: Latitudinal and topographical variabilities of free atmospheric turbulence  
738 from high-resolution radiosonde data sets, *J. Geophys. Res. Atmos.*, 124, 4283–  
739 4298. <https://doi.org/10.1029/2018JD029982>, 2019.

740 Zhang, J., J., Guo, H., Xue, S., Zhang, K., Huang, W. Dong, et al.: Tropospheric gravity

741 waves as observed by the high-resolution China radiosonde network and their  
742 potential sources, *J. Geophys. Res. Atmos.*, 127, e2022JD037174,  
743 <https://doi.org/10.1029/2022JD037174>, 2022.

744 Zhang, J., J., Guo, S., Zhang, and Shao, J.: Inertia-gravity wave energy and instability  
745 drive turbulence: Evidence from a near-global high-resolution radiosonde  
746 dataset, *Clim. Dyn.*, 58(11), 2927–2939, [https://doi.org/10.1007/s00382-021-](https://doi.org/10.1007/s00382-021-06075-2)  
747 06075-2, 2022.

748

749

750

751

752

753

754

755

756

757

758

759

760

761

762

763

764

765

766

767

768

769

770

带格式的: 缩进: 左侧: 0 厘米, 首行缩进: 0 厘米

771

772

773 **Table 1.** Comparisons of mean wind shears between HVRRS and ERA5 reanalysis at  
 774 heights of 0–2 km a.g.s.l. (a), 10–15 km a.g.s.l. (b), and 20–25 km a.g.s.l. (c).

**(a) Wind shear at 0–2 km a.g.s.l. (m/s/km)**

	Polar (NH)	Midlatitude (NH)	Subtropics (NH)	Tropics	Subtropics (SH)	Midlatitude (SH)	Polar (SH)
HVRRS	12.60 67	12.7294	12.1030	10.64 57	12.823.0 3	14.126	15.350 1
ERA5	8.027. 45	9.147.68	8.627.78	5.214	8.544	10.329.67	8.7342

**(b) Wind shear at 10–15 km a.g.s.l. (m/s/km)**

HVRRS	13.22 3	14.9571	13.3802	9.490	13.5228	14.664	13.110 0
ERA5	4.172 2	6.08.13	6.766.82	5.798 6	6.7486	5.1320	3.3842

**(c) Wind shear at 20–25 km a.g.s.l. (m/s/km)**

HVRRS	15.17 2	15.6674	15.2041	16.72 6	16.5769	16.12	17.195
ERA5	2.857	3.483.52	4.03.06	5.227	3.929	3.336	2.9092

775

776

777

778

779

780

781

782

783

784  
785  
786  
787  
788  
789  
790  
791  
792  
793  
794  
795  
796

**Table 2.** The occurrence rate of low  $Ri$  at 0.8–1.3 km a.g.s.l. (a), 2.2–3.2 km a.g.s.l. (b), 6–15 km a.g.s.l. (c), and 20–21 km a.g.s.l. (d). The critical  $Ri$  ( $Rit$ ) is 1/4 for radiosonde, and it increases from 1/4 to 2 for ERA5 reanalysis. Note that HVRRS data were vertically resampled to 100-m, 200-m, 300-m, and 400-m at these four height intervals to match with the ERA5 reanalysis. In addition, the moving average number in Eq.(1) is 0. RS stands for radiosonde.

<b>(a) Frequency of low <math>Ri</math> at 0.8–1.3 km a.g.s.l. (%) / Vertical resolution of RS is 100-m</b>							
	Polar (NH)	Midlatitude (NH)	Subtropics (NH)	Tropics	Subtropics (SH)	Midlatitude (SH)	Polar (SH)
RS, $Rit=1/4$	<u>14.76</u>	<u>22.764</u>	<u>22.1386</u>	<u>13.28</u>	<u>20.952</u>	<u>22.443</u>	<u>20.46</u>
	<del>5.20</del>	<del>5</del>		<del>92</del>	<del>9</del>		<del>77</del>
ERA5, $Rit=1/4$	<u>2.415</u>	<u>8.9388</u>	<u>6.307</u>	<u>2.324</u>	<u>6.9380</u>	<u>4.5247</u>	<u>2.964</u>
	<del>5</del>			<del>9</del>			
ERA5, $Rit=0.5$	<u>3.737</u>	<u>12.8006</u>	<u>9.463</u>	<u>3.605</u>	<u>11.954</u>	<u>8.42795</u>	<u>7.342</u>
							<del>2</del>
ERA5, $Rit=1$	8.54	<u>21.1022</u>	<u>22.1148</u>	<u>8.332</u>	<u>26.2345</u>	<u>19.4582</u>	<u>15.98</u>
				<del>7</del>		<del>1</del>	<del>78</del>
ERA5, $Rit=1.5$	<u>4.18</u>	<u>29.692</u>	<u>31.44</u>	<u>12.98</u>	<u>36.8807</u>	<u>28.8379</u>	<u>24.03</u>
	<u>13.80</u>			8		<del>7</del>	<del>3.22</del>
ERA5, $Rit=2$	<u>19.04</u>	<u>36.7858</u>	<u>38.5032</u>	<u>17.08</u>	<u>44.2137</u>	<u>38.0360</u>	<u>30.18</u>
	<del>44</del>			<del>20</del>	<del>2</del>	<del>0</del>	<del>29.68</del>

**(b) Frequency of low  $Ri$  at 2.2–3.2 km a.g.s.l. (%) / Vertical resolution of RS is 200-m**

RS, $R_{it}=1/4$	3.004	<del>5.606</del> 22	<del>7.409</del> 00	5.486	<del>8.879</del> 71	4.29	<del>4.123</del>
				7			98
ERA5, $R_{it}=1/4$	0.224	0.60	1.00	1.330	2.296	0.286	0.11
ERA5, $R_{it}=0.5$	0.37	1.03	1.96	2.10	4.232	0.50	0.18
ERA5, $R_{it}=1$	1.106	3.26	6.35	5.230	10.00	2.20	0.931
ERA5, $R_{it}=1.5$	2.647	6.75	12.320	9.020	16.391	5.620	2.68
	7						
ERA5, $R_{it}=2$	<del>5.024</del>	10.85	18.205	13.01	22.9045	9.874	5.10
	80			3			

**(c) Frequency of low  $R_i$  at 6–15 km a.g.s.l. (%) / Vertical resolution of RS is 300-m**

RS, $R_{it}=1/4$	0.756	2.204	3.8691	<del>6.005</del>	4.446	1.98	0.569
				98			
ERA5, $R_{it}=1/4$	0.170	0.38	0.54	1.476	0.576	0.254	0.05
ERA5, $R_{it}=0.5$	0.32	1.16	1.95	4.376	2.10	0.93	0.15
ERA5, $R_{it}=1$	1.387	4.33	7.732	13.14	8.9089	3.521	0.61
ERA5, $R_{it}=1.5$	2.93	8.321	14.54	21.79	17.05	6.76	1.38
				8			
ERA5, $R_{it}=2$	4.70	12.35	20.91	29.28	24.55	10.02	2.32

**(d) Frequency of low  $R_i$  at 20–21 km a.g.s.l. (%) / Vertical resolution of RS is 400-m**

RS, $R_{it}=1/4$	0.03	0.07	0.123	0.04	0.04	0.10	0.07
ERA5, $R_{it}=1/4$	0.01	0.02	0.01	0.02	0.02	0.03	0.04
ERA5, $R_{it}=0.5$	0.02	0.03	0.01	0.02	0.03	0.04	0.04
ERA5, $R_{it}=1$	0.03	0.05	0.04	0.05	0.05	0.08	0.04
ERA5, $R_{it}=1.5$	0.04	0.11	0.13	0.19	0.09	0.17	0.04
ERA5, $R_{it}=2$	0.05	0.21	0.32	0.55	0.18	0.30	0.05

797

798

799

800

801  
802  
803  
804  
805  
806  
807  
808  
809  
810  
811  
812  
813  
814  
815  
816  
817  
818  
819  
820  
821  
822  
823  
824  
825  
826

827 **Table 3.** Vertical wind shears at 0.8–1.3 km a.gs.l. (a), 2.2–3.2 km a.gs.l. (b), 6–15 km  
828 a.gs.l. (c), and 20–21 km a.gs.l. (d). Note that HVRRS data was vertically resampled to  
829 100-m, 200-m, 300-m, and 400-m at these four height intervals to match with the ERA5  
830 reanalysis. RS stands for radiosonde.

**(a) Wind shear at 0.8–1.3 km a.g.s.l. (m/s/km) / Vertical resolution of RS is 100-m**

	Polar (NH)	Midlatitude (NH)	Subtropics (NH)	Tropics	Subtropics (SH)	Midlatitude (SH)	Polar (SH)
RS	12.50	<del>11.893</del> 6	<del>11.298</del> 0	<del>11.51</del>	<del>13.325</del> 4	13.06	<del>13.85</del>
		3		9.83			14.04
ERA5	<del>5.504</del>	<del>6.145</del> 92	<del>6.674</del> 7	<del>4.928</del>	<del>7.092</del>	<del>7.006</del> 71	<del>6.230</del>
	3			3			5

**(b) Wind shear at 2.2–3.2 km a.g.s.l. (m/s/km) / Vertical resolution of RS is 200-m**

RS	<del>8.263</del>	<del>9.009</del>	<del>9.112</del> 4	<del>8.679</del>	<del>9.224</del> 5	<del>9.399</del>	<del>9.751</del>
	1			08			0.00
ERA5	<del>3.702</del>	<del>4.504</del> 7	<del>5.251</del> 9	<del>4.675</del>	<del>5.441</del>	<del>4.731</del>	<del>4.201</del>
							9

**(c) Wind shear at 6–15 km a.g.s.l. (m/s/km) / Vertical resolution of RS is 300-m**

RS	8.30	<del>9.580</del>	<del>9.544</del> 1	<del>7.762</del>	<del>9.880</del>	9.38	<del>8.060</del>
ERA5	<del>4.010</del>	<del>5.392</del> 2	<del>6.025</del> 84	<del>5.261</del>	<del>6.321</del> 4	<del>4.867</del> 6	<del>3.397</del>

**(d) Wind shear at 20–21 km a.g.s.l. (m/s/km) / Vertical resolution of RS is 400-m**

RS	<del>9.072</del>	<del>10.374</del> 0	<del>11.556</del> 7	<del>12.50</del>	<del>11.992</del> 1	10.48	<del>9.948</del>
				6	4		0
ERA5	<del>2.993</del>	<del>3.853</del>	<del>4.807</del> 9	<del>5.635</del>	<del>4.732</del>	<del>3.643</del>	2.98
	00			9			

831  
832  
833  
834  
835  
836  
837  
838



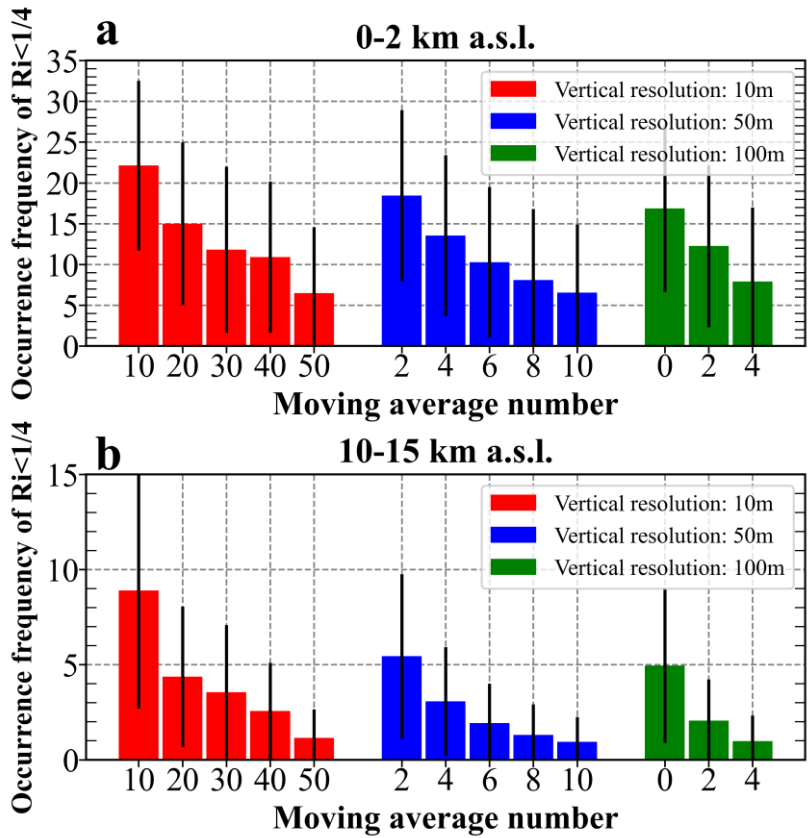
839  
840  
841  
842  
843  
844  
845  
846  
847  
848

849 **Table 4.** Similar to Tab.1 but for the occurrence frequency of  $Ri < Rit$ . Note that  $Rit$  is  
850 indicated by  $Ri < 1/4$  in radiosonde, but it is identified with 1 in ERA5 reanalysis.

<b>(a) <math>OF(Ri &lt; Rit)</math> at 0–2 km a.g.s.l. (%)</b>							
	Polar (NH)	Midlatitude (NH)	Subtropics (NH)	Tropics	Subtropics (SH)	Midlatitude (SH)	Polar (SH)
HVRRS	<del>9.0556</del>	<del>15.5761</del>	<del>16.4457</del>	13.130	<del>17.30698</del>	<del>15.2138</del>	<del>13.40</del>
		0	8	8			97
ERA5	<del>28.026</del>	<del>41.2633</del>	<del>40.3635</del>	<del>40.143</del>	<del>47.45056</del>	<del>42.92046</del>	<del>27.59</del>
	91	85	70	7.27			6.55
<b>(b) <math>OF(Ri &lt; Rit)</math> at 10–15 km a.g.s.l. (%)</b>							
HVRRS	<del>0.513</del>	<del>2.0522</del>	<del>5.2144</del>	11.112	<del>6.0017</del>	<del>1.535</del>	<del>0.652</del>
				2			
ERA5	0.44	2.62	6.86	17.03	7.15	1.67	0.28
<b>(c) <math>OF(Ri &lt; Rit)</math> at 20–25 km a.g.s.l. (%)</b>							
HVRRS	<del>0.4536</del>	<del>0.489</del>	<del>0.423</del>	0.51	<del>0.3840</del>	0.67	<del>1.533</del>
							5
ERA5	0.06	0.07	0.04	0.11	0.06	0.06	0.04

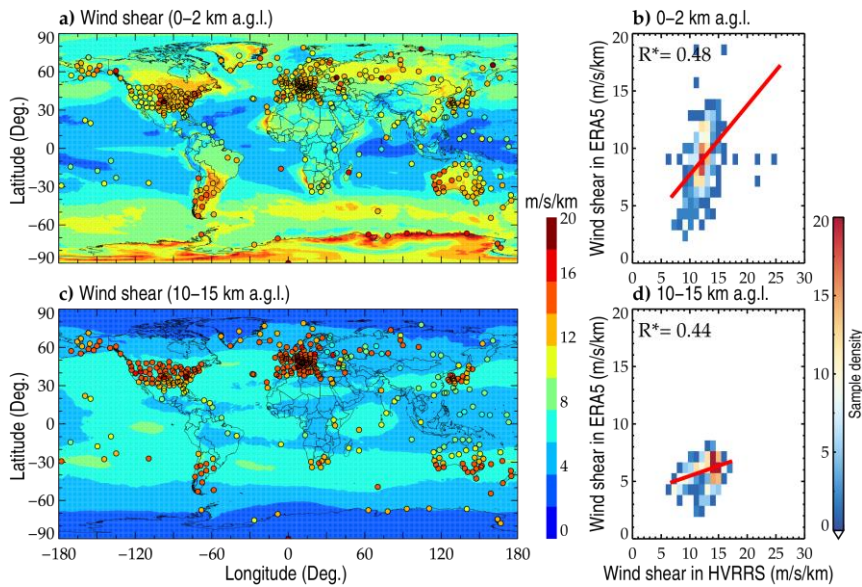
851  
852

853  
854  
855  
856  
857  
858  
859  
860  
861  
862  
863  
864  
865  
866

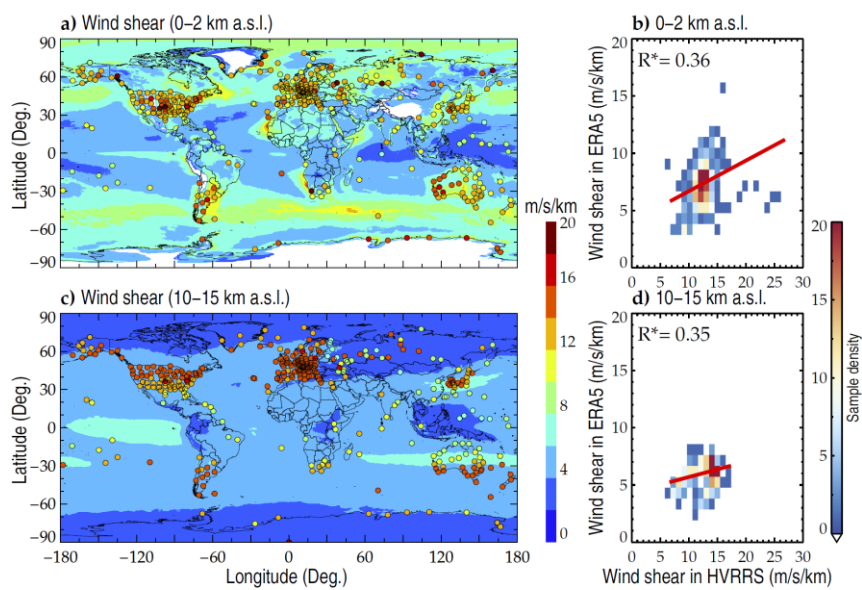


867  
 868 **Figure 1.** The averaged occurrence frequencies of  $Ri < 1/4$  at heights of 0–2 km a.s.l. (a)  
 869 and 10–15 km a.s.l. (b), with vertical resolutions ranging 10-m to 100-m and moving  
 870 point numbers increasing from 0 to 50. The error bars correspond to the standard  
 871 deviation. The metrics are counted based on all radiosonde profiles during years 2017–  
 872 2022.

873  
 874



875

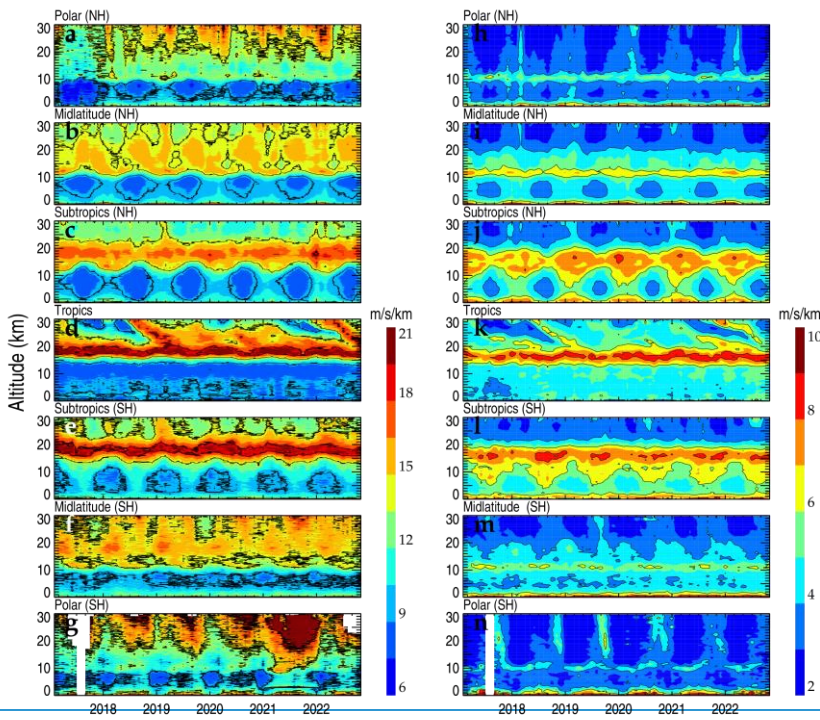


876

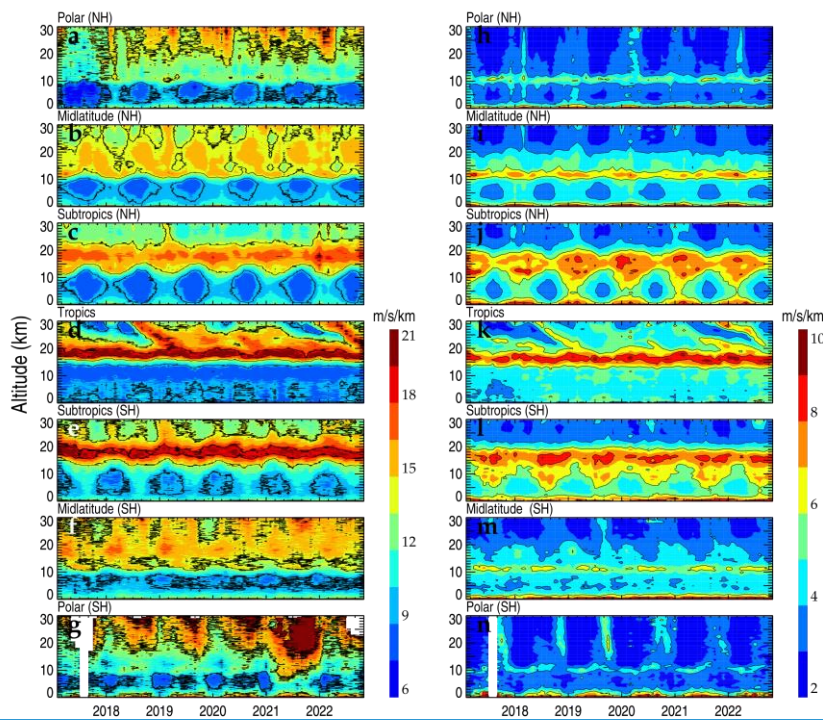
877 **Figure 2.** The spatial distribution of mean wind shear in ERA5 reanalysis at heights of  
 878 0–2 km a.g.s.l. (a) and 10–15 km a.g.s.l. (c), where the areas with a near surface pressure  
 879 lower than 800 hPa are masked with white. The overlaid colored circles represent the  
 880 result in HVRRS at the same height levels. Each data point represents a vertically

881 averaged value of the wind shear at one radiosonde station during the whole study  
 882 period. Density plots (b, d) show the correlation between wind shears in HVRRS and  
 883 ERA5 reanalysis. The ERA5 derived wind shears are spatially and temporally  
 884 collocated with those of HVRRS. In addition, the red lines represent a least-squared  
 885 linear regression, and the star superscripts indicate that values are statistically  
 886 significant ( $p < 0.05$ ).

887  
 888

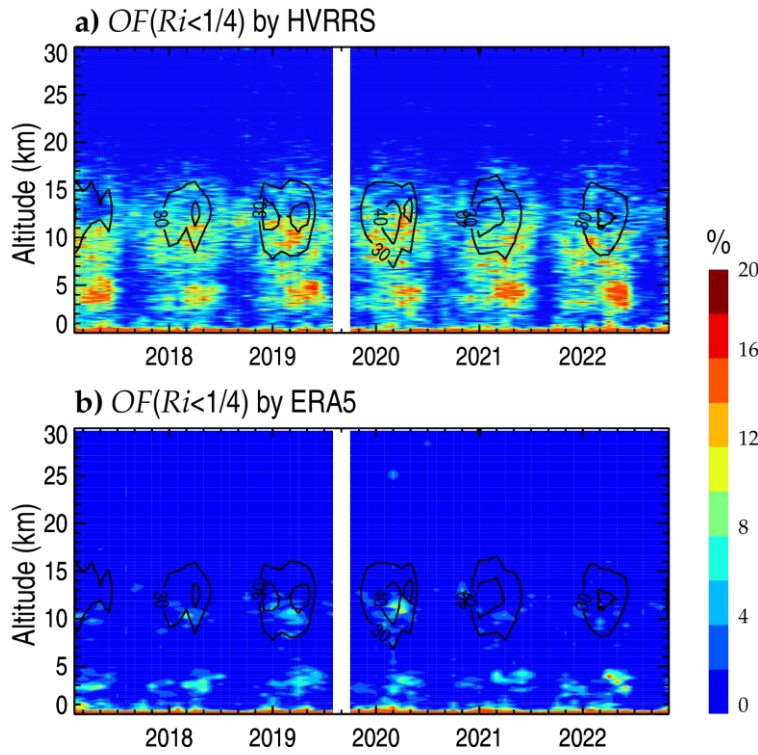


889



890

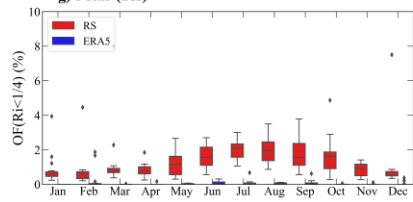
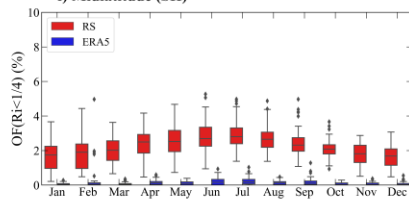
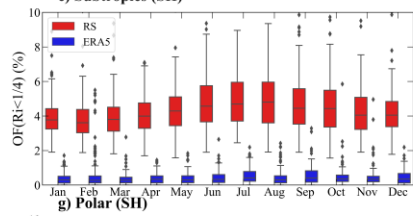
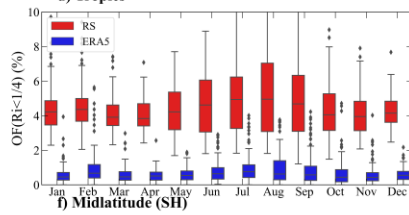
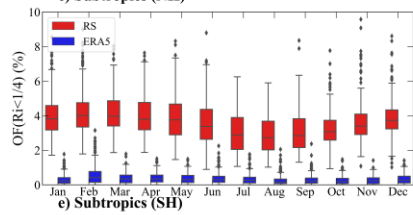
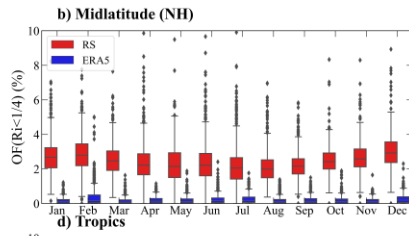
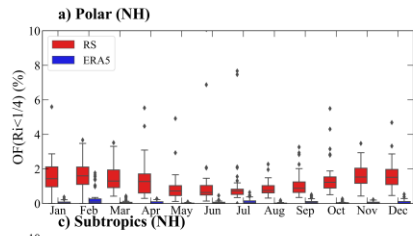
891 **Figure 3.** Monthly mean wind shears during years 2017–2022 in HVRRS (a–g) and  
 892 ERA5 reanalysis (h–n) at different climate zones. The ERA5 derived wind shears are  
 893 spatially and temporally collocated with those of HVRRS. NH=Northern Hemisphere;  
 894 SH=Southern Hemisphere.



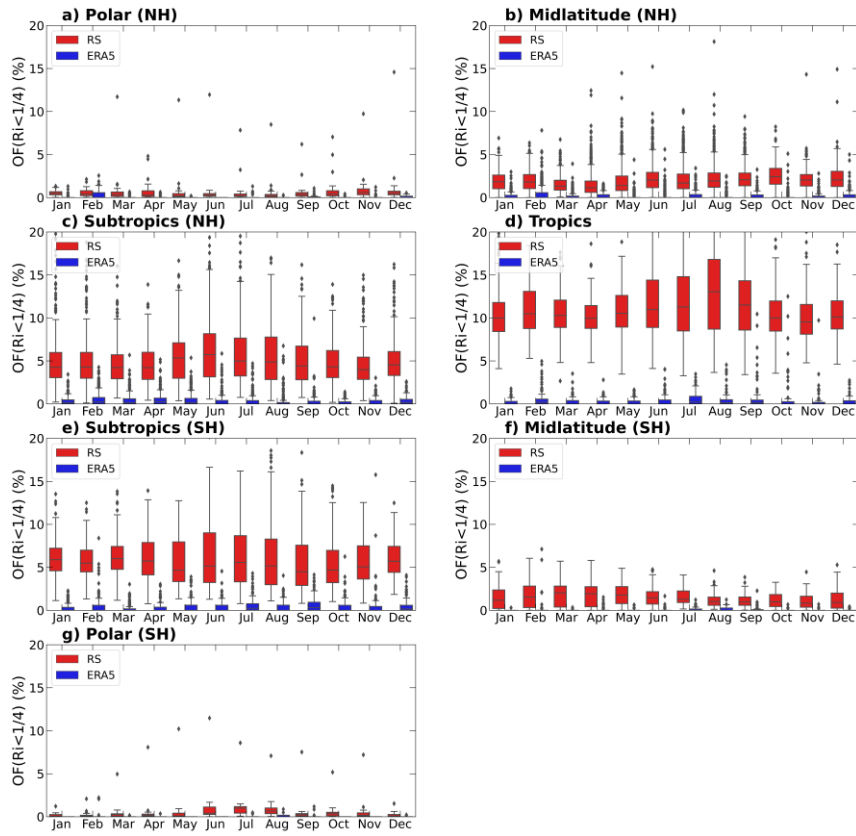
895

896 **Figure 4.** The monthly occurrence frequency of  $Ri < 1/4$  at Corpus Christi station ( $27.77^\circ$   
 897  $N$ ,  $-97.5^\circ W$ ) in HVRRS (a) and ERA5 reanalysis (b). Note that the contour curves in  
 898 (a) and (b) concern the mean horizontal wind speed, and that the ERA5 derived  
 899 quantities are spatially and temporally collocated with those of HVRRS.



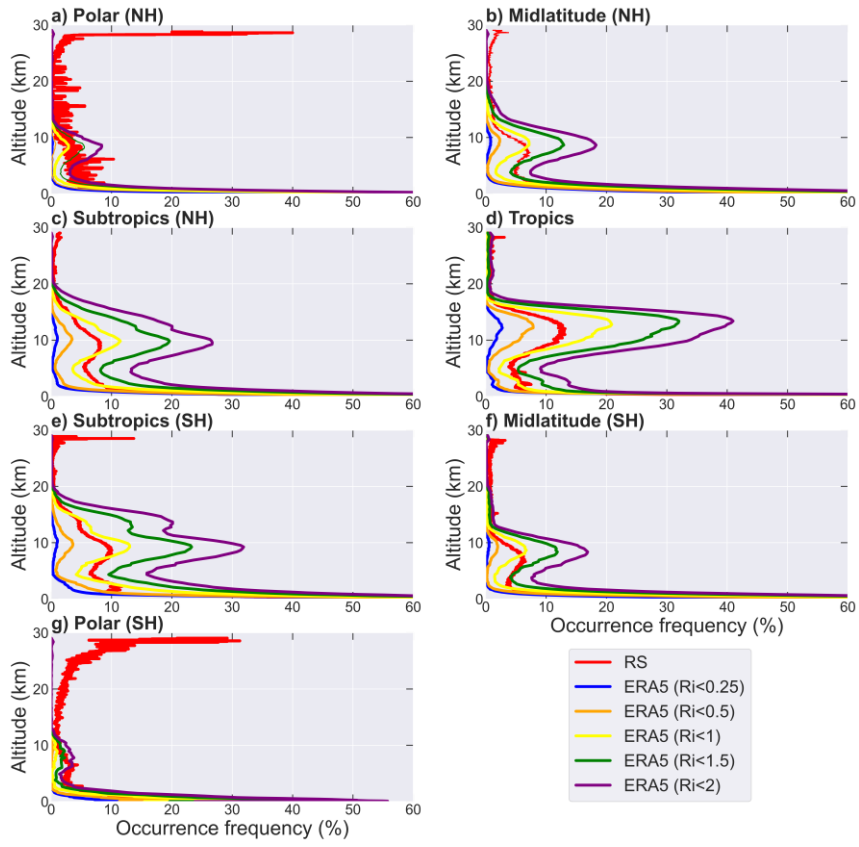




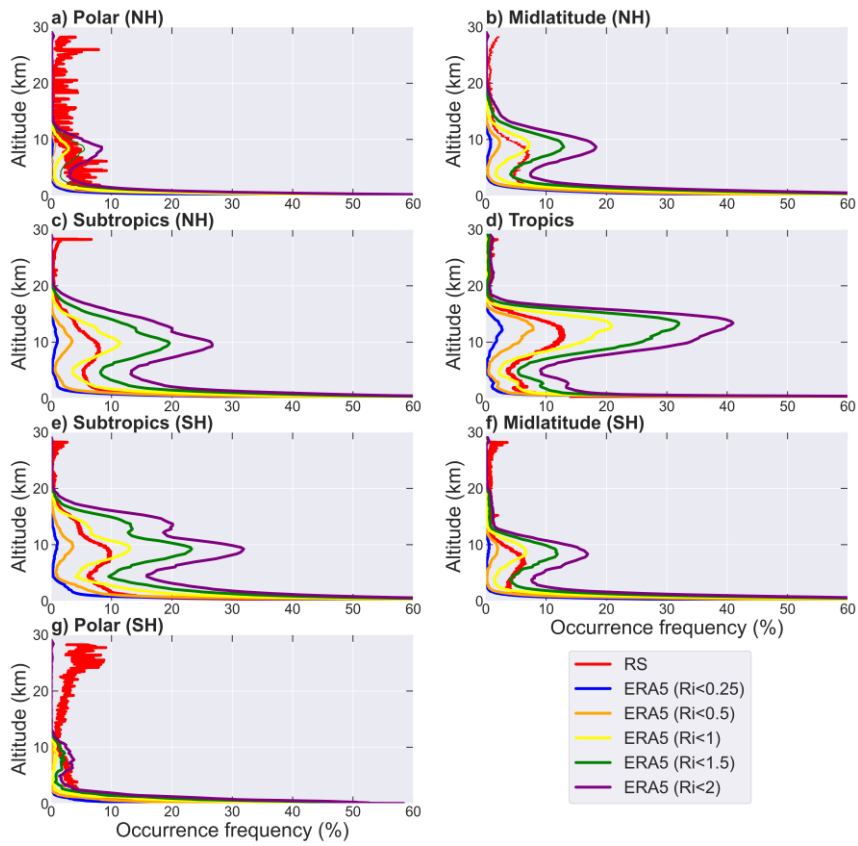


901

902 **Figure 5.** The annual cycles of the occurrence frequency of  $Ri < 1/4$  in different climate  
 903 zones ~~at 10–15 km a.g.l.~~ ~~at 10–15 km a.g.s.l.~~. The red and blue boxes represent the  
 904 frequencies in HVRRS and ERA5 reanalysis, respectively. The ERA5 derived  $Ri$  is  
 905 spatially and temporally collocated with that of HVRRS. NH, Northern Hemisphere;  
 906 SH, Southern Hemisphere.

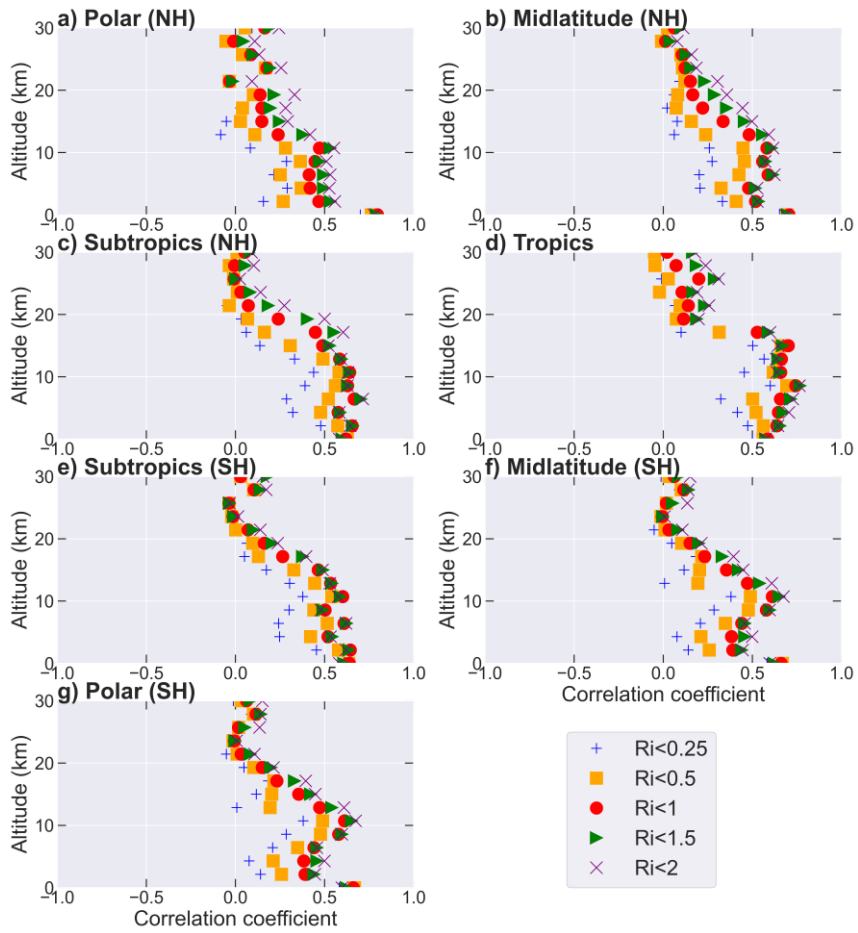


907

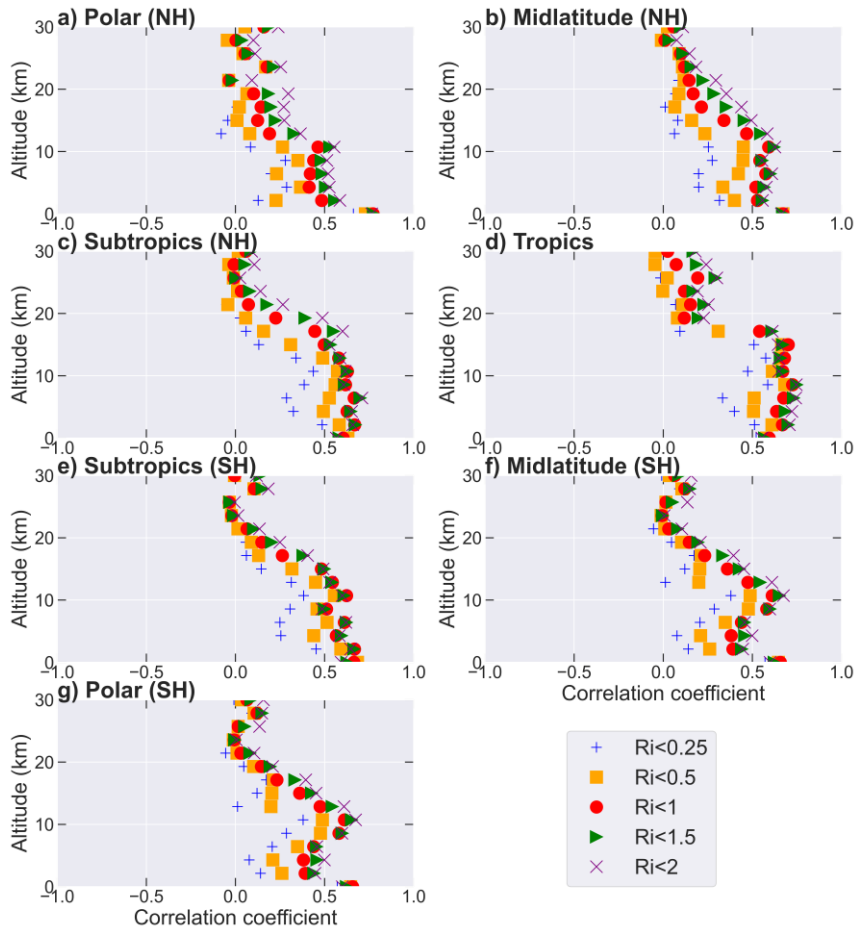


908

909 **Figure 6.** The altitude variation of the occurrence frequency of  $Ri$  below certain  
 910 thresholds (0.25, 0.5, 1, 1.5, and 2) in ERA5 reanalysis in various climate zones. The  
 911 ERA5 derived  $Ri$  is spatially and temporally collocated with that of HVRRS. The  
 912 occurrences of  $Ri < 1/4$  in HVRRS are overlapped with red lines.

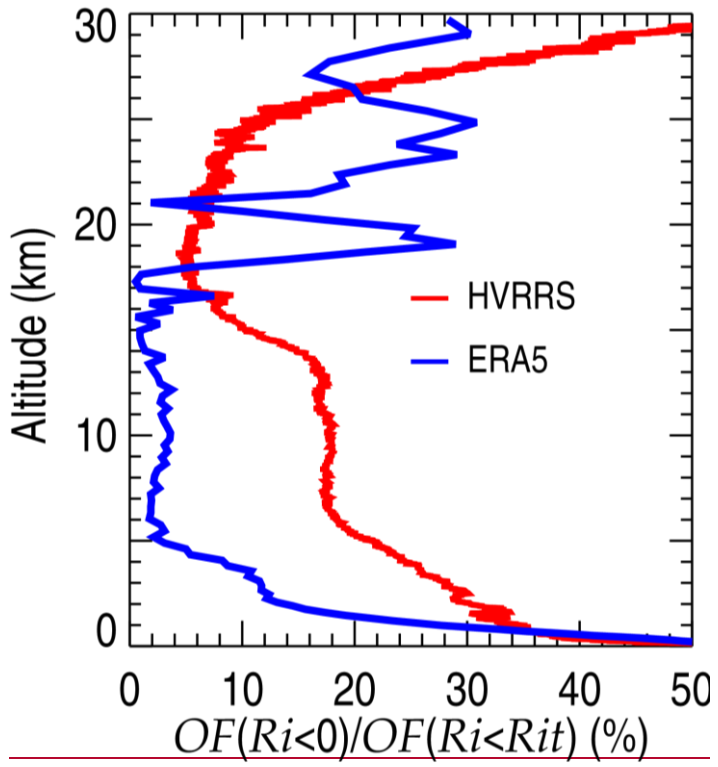


913

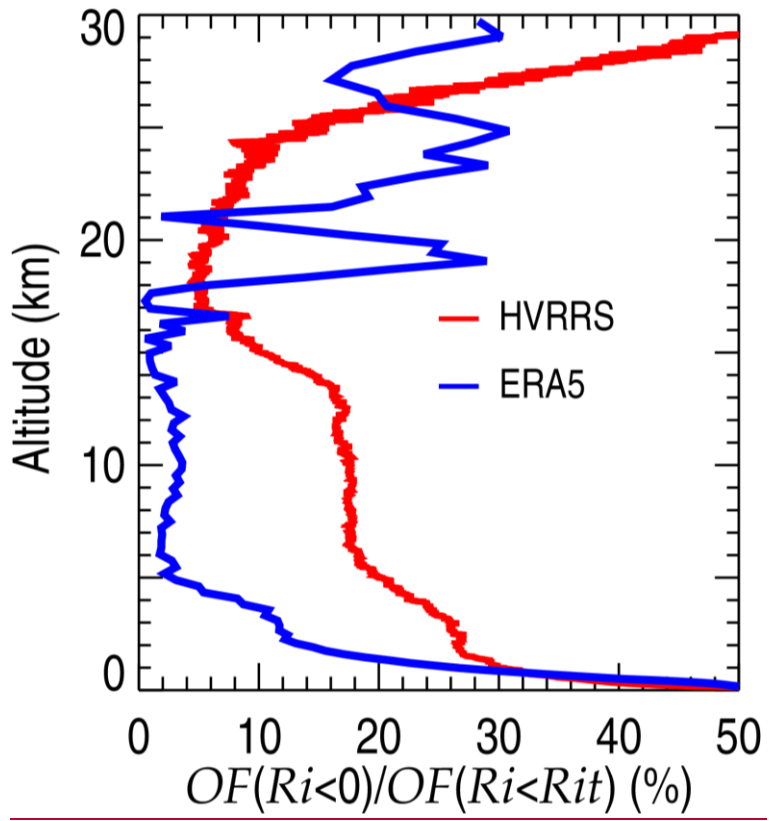


914

915 **Figure 7.** The correlation coefficients between monthly averaged occurrence frequency  
 916 of  $Ri < 1/4$  in the HVRRS and the monthly occurrence frequency of  $Ri$  below certain  
 917 thresholds (0.25, 0.5, 1, 1.5, and 2) in ERA5 reanalysis. The ERA5 derived  $Ri$  is  
 918 spatially and temporally collocated with that of HVRRS. The coefficients in various  
 919 climate zones are estimated in an increment of 2 km.



920



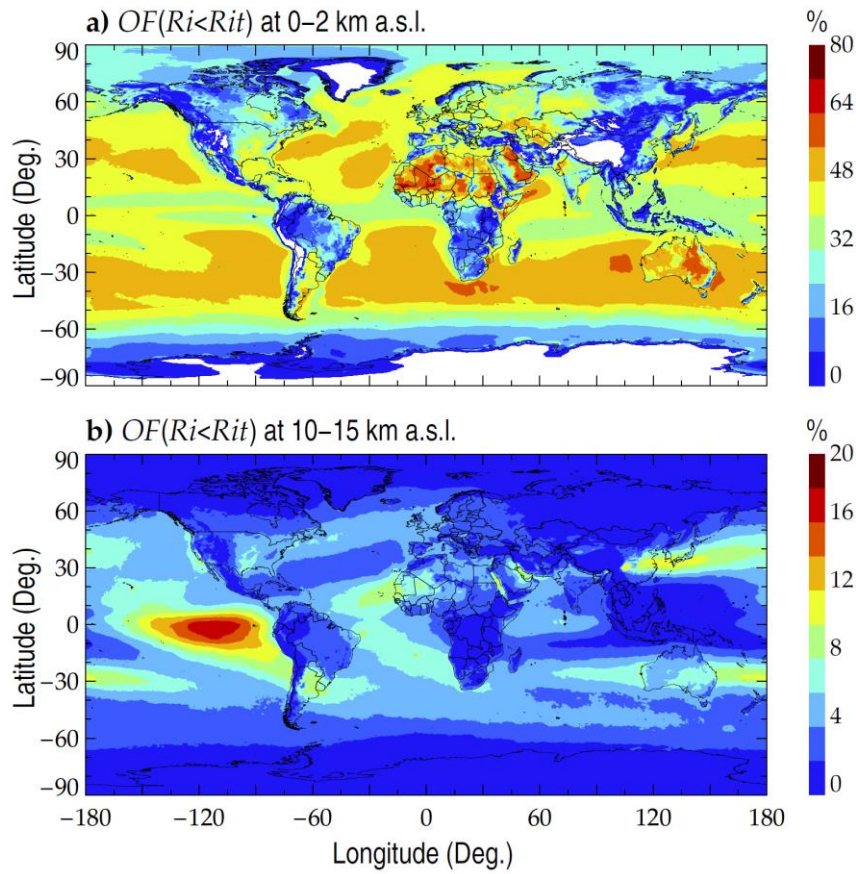
921

922 **Figure 8.** The percentage of  $OF(Ri<0)$  relative to  $OF(Ri<Rit)$  in HVRRS (red) and  
 923 ERA5 reanalysis (blue).

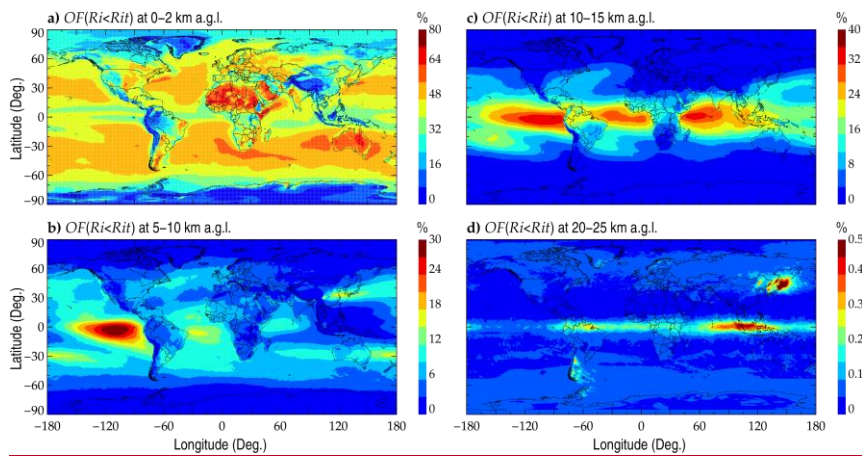
924

925

926



927



928

929 **Figure 9.** The spatial distribution of the mean  $OF(Ri < Rit)$  in ERA5 reanalysis at 0–2  
 930 km a.g.s.l. (a) and 5–10–105 km a.g.s.l. (b), 10–15 km a.g.l. (c), and 20–25 km a.g.l.

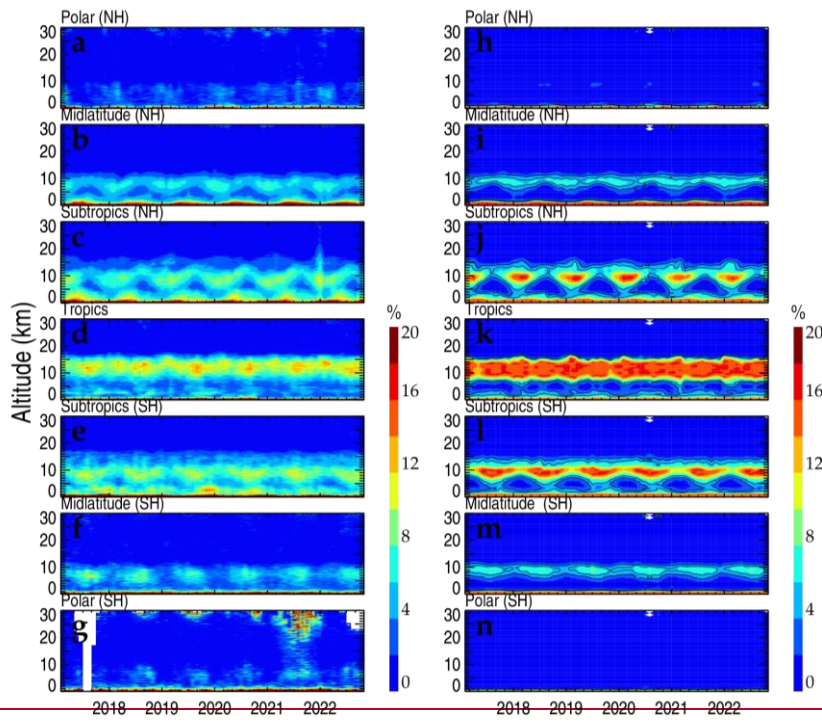


931 (d). Note that *Rit* is set to 1.

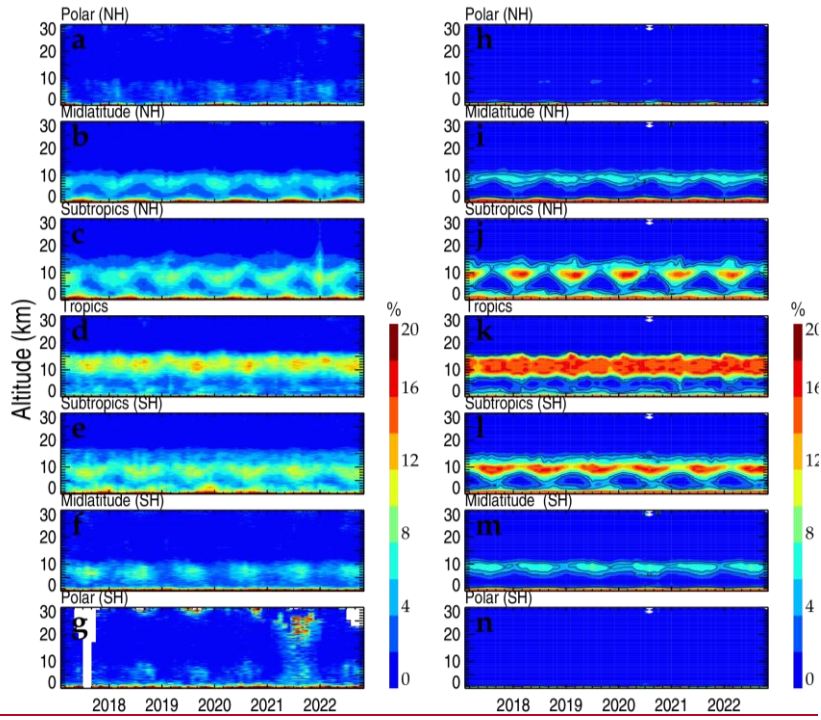
932

933

934

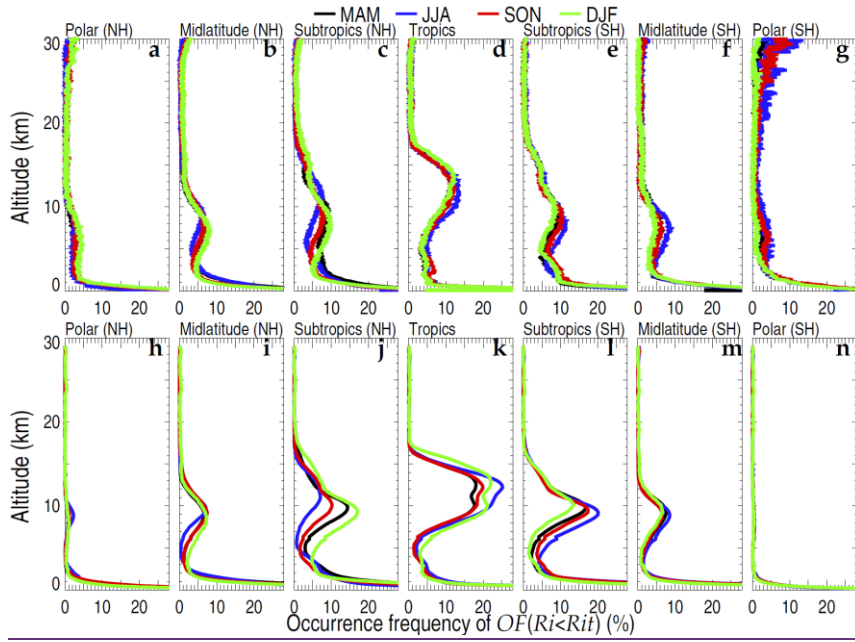


935

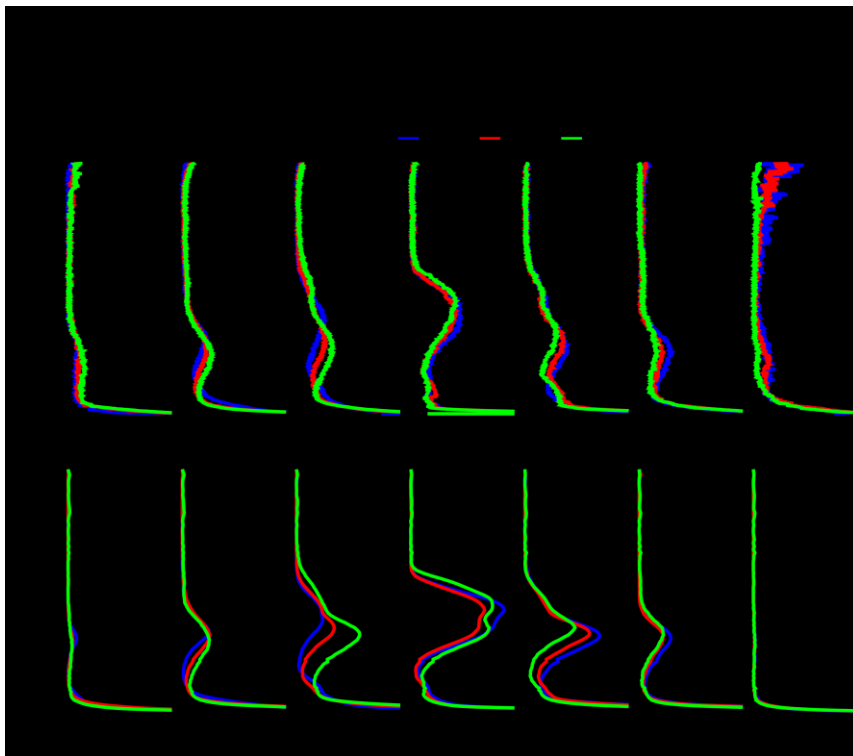
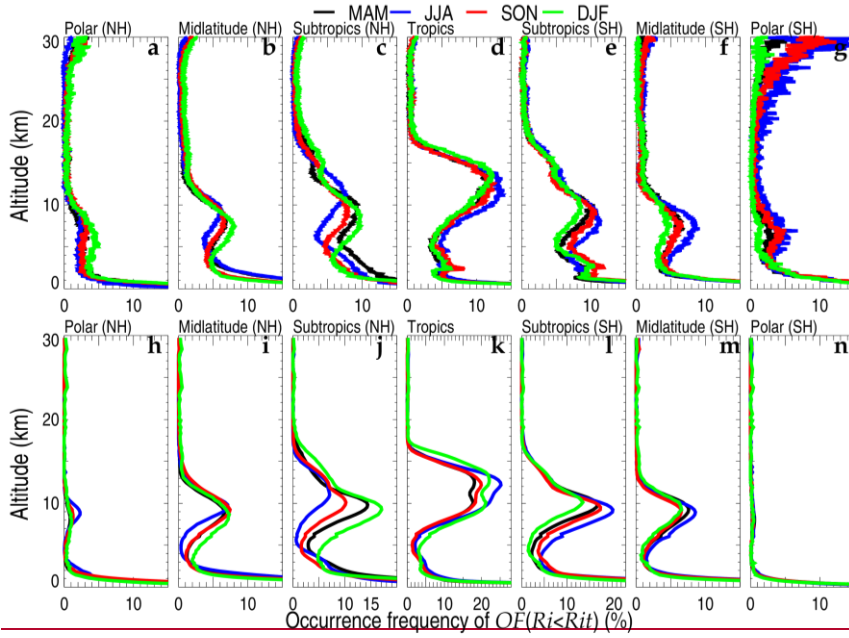


936

937 **Figure 10.** The monthly averaged  $OF(Ri < Rit)$  in the HVRRS (a–g) and ERA5  
 938 reanalysis (h–n) in seven climate zones. NH=Northern Hemisphere; SH=Southern  
 939 Hemisphere.

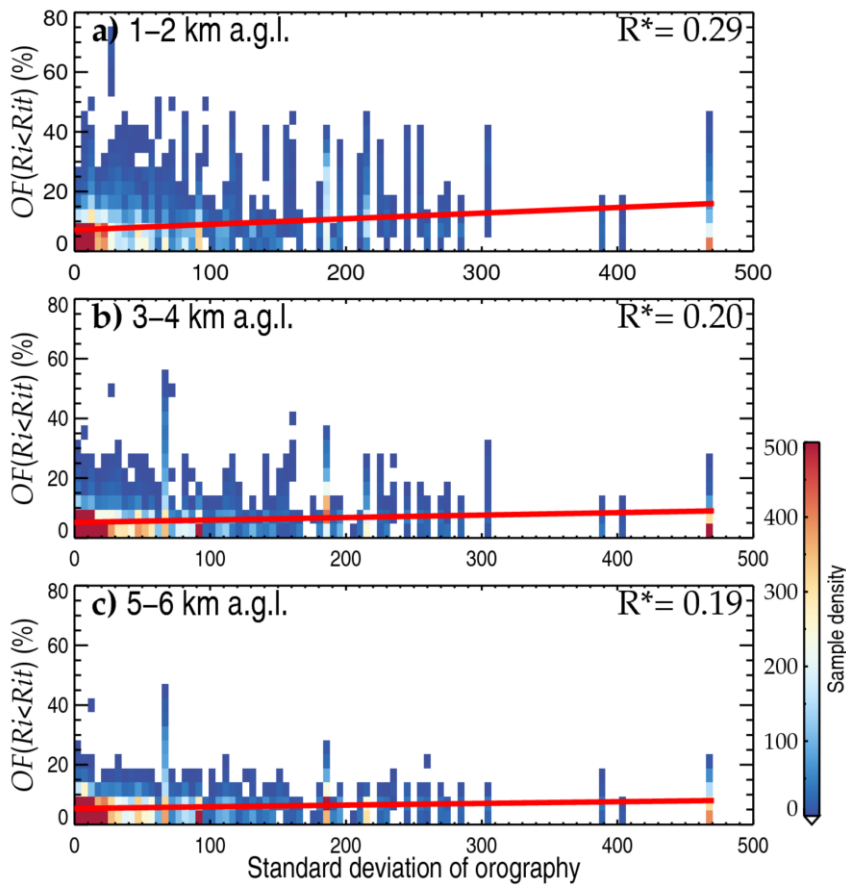


940



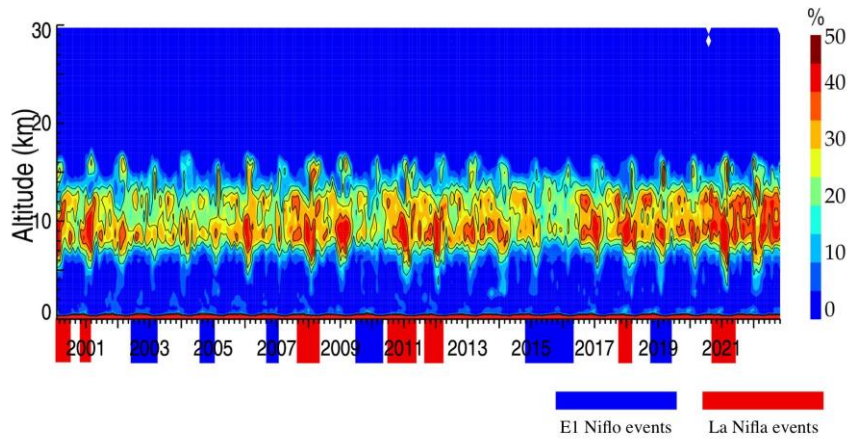
带格式的: 字体: (中文) Times New Roman, 0 磅, (无), 字符  
 缩放: 0%, 不对齐到网格, 边框: (无框线), 图案: 清除 (黑色)

944 **Figure 11.** The seasonal averaged  $OF(Ri < Rit)$  in the HVRRS (a–g) and ERA5  
 945 reanalysis (h–m) in seven climate zones. MAM, March–April–May; JJA, June–July–  
 946 August; SON, September–October–November; DJF, December–January–February.  
 947 NH=Northern Hemisphere; SH=Southern Hemisphere.



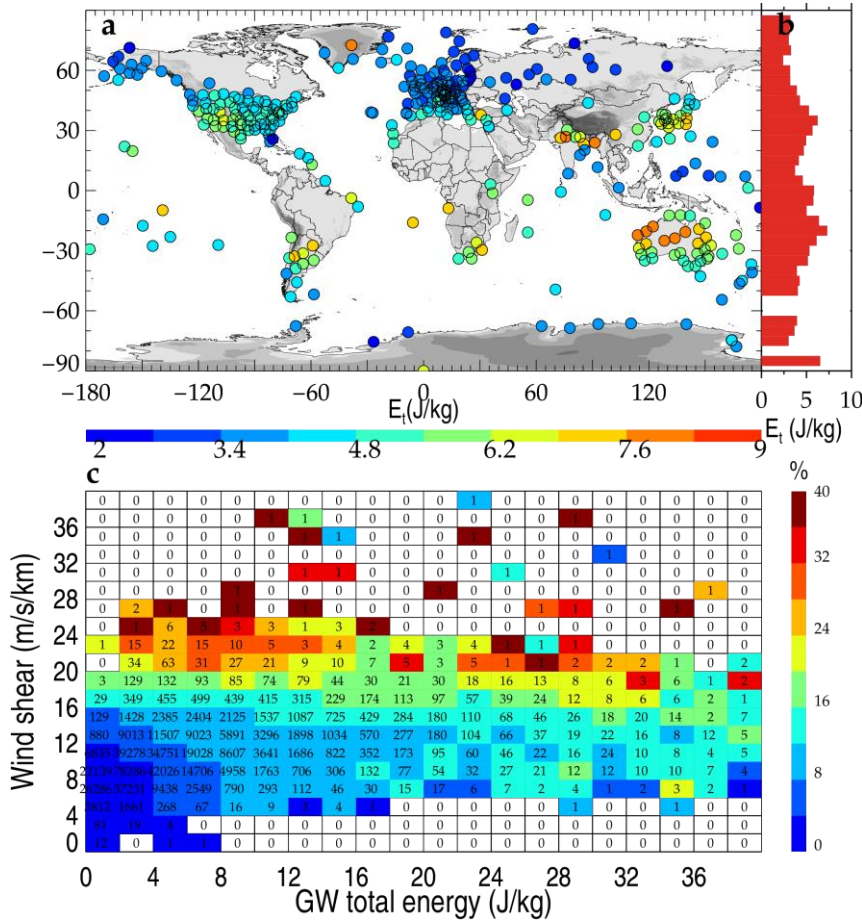
948 **Figure 12.** The association of HVRRS-determined  $OF(Ri < Rit)$  with different standard  
 949 deviations of orography (dimensionless). (a), (b), and (c) are for height ranges of 1–2  
 950 km, 3–4 km, and 5–6 km a.g.l., respectively. The correlation coefficients between  
 951  $OF(Ri < Rit)$  and standard derivation of orography are marked in the top right corner,  
 952 where the star superscripts indicate that values are statistically significant ( $p < 0.05$ ).  
 953

954



955

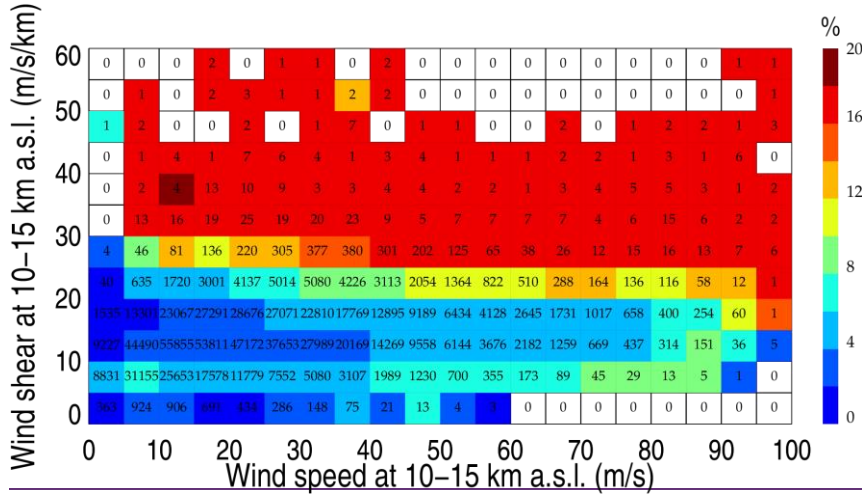
956 **Figure 13.** The monthly averaged  $OF(Ri < Rit)$  in ERA5 reanalysis over the Niño 3  
957 region ( $5^{\circ}\text{N} - 5^{\circ}\text{S}$ ,  $150^{\circ}\text{W} - 90^{\circ}\text{W}$ ). The blue and red shadings in time axis indicate the  
958 time periods with El Niño and La Niña events, respectively.



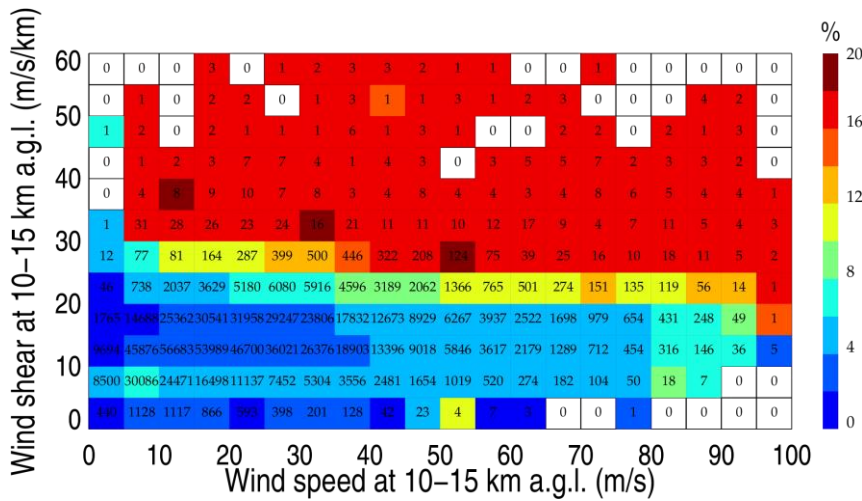
959  
 960 **Figure 14.** Geographical distribution of mean tropospheric GW total energy obtained  
 961 from the HVRRS (a). The latitudinal variation of mean energy in a grid cell of 5°  
 962 latitude (b). The joint distribution of  $OF(Ri < Rit)$  with GW energy and wind shear (c).  
 963 The  $OF(Ri < Rit)$  and wind shear are derived from individual HVRRS profiles and  
 964 vertically averaged over the tropospheric segment that is used for GW study. The  
 965 numerical number in (c) indicates the matched profile number in each grid, using a bin  
 966 size of 2 J/kg along the x axis and 2 m/s/km along the y axis.



967



968



969 **Figure 15.** Joint distribution of HVRRS-derived wind speed, wind shear, and  
 970  $OF(Ri < Rit)$ , with a bin size of 5 m/s along the x axis and 5 m/s/km along the y axis.  
 971 Note that all the relationship is based on the mean result of individual profiles at heights  
 972 of 10–15 km a.g.s.l.. The number indicates the matched profile number in each grid.